# The Shanderman eclogites: a Late Carboniferous high-pressure event in the NW Talesh Mountains (NW Iran)

Stefano Zanchetta, Andrea Zanchi, Igor Villa, Stefano Poli and Giovanni Muttoni

*Geological Society, London, Special Publications* 2009; v. 312; p. 57-78
doi:10.1144/SP312.4

# The Shanderman eclogites: a Late Carboniferous high-pressure event in the NW Talesh Mountains (NW Iran)

STEFANO ZANCHETTA[1]*, ANDREA ZANCHI[1], IGOR VILLA[1,3], STEFANO POLI[2] & GIOVANNI MUTTONI[2]

[1]*Dipartimento Scienze Geologiche e Geotecnologie, Università di Milano-Bicocca, Piazza della Scienza 4, Milano, 20126 Italy*

[2]*Dipartimento di Scienze della Terra, Università di Milano, Via Mangiagalli 34, 20133 Milano, Italy*

[3]*Institut für Geologie, Universität Bern, 3012 Bern, Switzerland*

**Corresponding author (e-mail: stefano.zanchetta@unimib.it)*

**Abstract:** The Shanderman Metamorphic Complex, exposed along the Caspian foothills of the Talesh Mountain, western Alborz, Iran, has always been interpreted as an ophiolitic fragment of the Palaeotethys Ocean. According to our new data, this unit consists of metamorphic rocks mainly represented by garnet–staurolite micaschists with large bodies of metabasites containing well-preserved eclogitic-phase assemblages. The Shanderman Complex (SC) was later intruded at middle crustal levels by intermediate–basic intrusive bodies. New Ar/Ar ages of paragonitic white micas in equilibrium with the high-pressure assemblages have given a Late Carboniferous age (315 $\pm$ 9 Ma). Our new data suggest that the SC was equilibrated in high-pressure conditions during an orogenic event that predates the Eo-Cimmerian orogeny by more than 100 Ma and that may be tentatively ascribed to the Variscan orogeny *sensu latu*. We suggest that the Shanderman Complex represents a fragment of the Upper Palaeozoic European continental crust. The occurrence of eclogites in these regions can be explained by two different hypotheses: (1) the SC high-pressure rocks can be related to the accretion of Gondwana-related Transcauscasian–Moesian microplate to the southern margin of Eurasia; or (2) the SC eclogites can represent a fragment of the Late Palaeozoic 'Variscan belt' *sensu latu* of central Europe, which has been translated eastwards during Permian along a dextral megashear zone taking from a Pangea-B to a Pangea-A plate configuration. This metamorphic unit was stacked southwards on the northern edge of the Iran Plate during the Eo-Cimmerian events occurring at the end of the Triassic. The eclogite-bearing basement of the SC was finally exhumed at the end of the Eo-Cimmerian orogeny, as suggested by the composition of the basal layers of the Shemshak Group dated here Middle Jurassic, that cover the crystalline rocks of the SC along a regional non-conformity. The SC was probably displaced further southwards during the Mesozoic opening of the South Caspian Basin and the Tertiary thrust stacking and dextral shearing accompanying the formation of the Alborz intracontinental belt.

**Supplementary material:** Available at http://www.geolsoc.org.uk/SUP18342.

Since the first reconstructions concerning the early Mesozoic evolution of Iran (Stöcklin 1968, 1974), the region between the northern flank of the Alborz Mountains and the South Caspian Sea coast has been interpreted as the trace of the Gondwana-related Iran Plate collision with the southern Eurasian margin (Sengör 1979, 1984, 1990; Berberian & King 1981; Alavi 1996; Brunet *et al.* 2003). The collision of Iran and of other 'Cimmerian' blocks against southern Asia resulted in the Eo-Cimmerian orogeny, the most relevant collision process affecting Eurasia between the end of the Triassic and the beginning of the Jurassic, which led to the definitive closure of the Palaeozoic Palaeotethys Ocean.

The main evidence for the Palaeotethys suture is exposed in the southern part of the Kopeh Dagh belt, between the city of Mashad and the Afghan–Turkmenistan border to the east (Alavi 1991; Ruttner 1993; Alavi *et al.* 1997). Here a Permo-Triassic accretionary wedge and Triassic volcanic arc successions separate Upper Palaeozoic slightly metamorphosed volcaniclastic units, belonging to the southern part of the Turan region, from the Gondwanan Palaeozoic succession of central Iran to the south. West of Mashad the suture zone is masked by Meso-Cenozoic sediments unconformably covering the Eo-Cimmerian structures. According to Alavi (1996), 'Palaeotethys remnants' discontinuously crop out close to the Iranian coast

*From*: BRUNET, M.-F., WILMSEN, M. & GRANATH, J. W. (eds) *South Caspian to Central Iran Basins*. The Geological Society, London, Special Publications, **312**, 57–78.
DOI: 10.1144/SP312.4 0305-8719/09/$15.00 

of the Caspian Sea in the Gorgan region and west of Rasht in Talesh Mountains, marking the position of the Palaeotethys suture and its general continuity along the northern edge of the Iran Plate.

The Talesh Mountains of northwestern Iran are thus a key area to investigate the location and evolution of the Eo-Cimmerian collisional zone. The peculiar rock association of metabasites with serpentinized ultramafic rocks present in the Shanderman Complex (Davies *et al.* 1972; Clark *et al.* 1975), cropping out along the Caspian foothills west of the towns of Masal and Shanderman, has been generally interpreted as a possible fragment of the Palaeotethys lithosphere (Sengör 1990; Alavi 1996) and has been considered as one of the main pieces of evidence of the Palaeotethys collision zone.

In this work we revise in detail the meaning of the Shanderman Complex in terms of lithological composition, geochemistry and metamorphic evolution, in order to understand if it can be really considered as an ophiolitic fragment. In fact, our new findings of previously unknown eclogites associated to garnet metapelites, later intruded by intermediate-mafic intrusive bodies, suggest a continental-crustal affinity of this unit rather than an oceanic origin. New Ar/Ar radiometric ages obtained on high-pressure white micas have given a Late Carboniferous age for the eclogitic peak, which suggests that high-pressure conditions are related to an earlier orogenic cycle, before the Cimmerian event. The origin of the Shanderman Complex, interpreted as a possible allochthonous nappe, from the Transcaucasian region and emplaced along the northern edge of the Iranian Plate during the Eo-Cimmerian orogeny is also discussed in this paper.

## The geological setting of the Talesh Mountains and its tectonic evolution

The Talesh Mountains, extending from Azerbaijan to the Sefid Rud south of Rasht, form the western part of the Alborz mountain system and flank the southwestern coast of the South Caspian Sea (Fig. 1). The belt has a sinuous shape, trending around east–west in Azerbaijan, turning north–south along the southwestern Caspian coast, and finally trending WSW–ENE west of Rasht. The Azerbaijan side of the belt, consisting of Tertiary – mainly Eocene – sedimentary and volcanic successions, has been described by Vincent *et al.* (2005). They interpret the Eocene evolution of this area in terms of back-arc extension or transtension following the Mesozoic opening of the South Caspian Basin to the north of the Neotethys subduction zone. The change to a compressional regime forming a high topographic relief occurred during the Oligocene and is marked by the deposition of coarse-grained siliciclastic deposits.

The Iranian part of the belt, about 50 km in width, is more complex, and consists mainly of a strongly deformed and discontinuous sedimentary succession spanning the entire Phanerozoic time. A few slices of metamorphic rocks grouped into

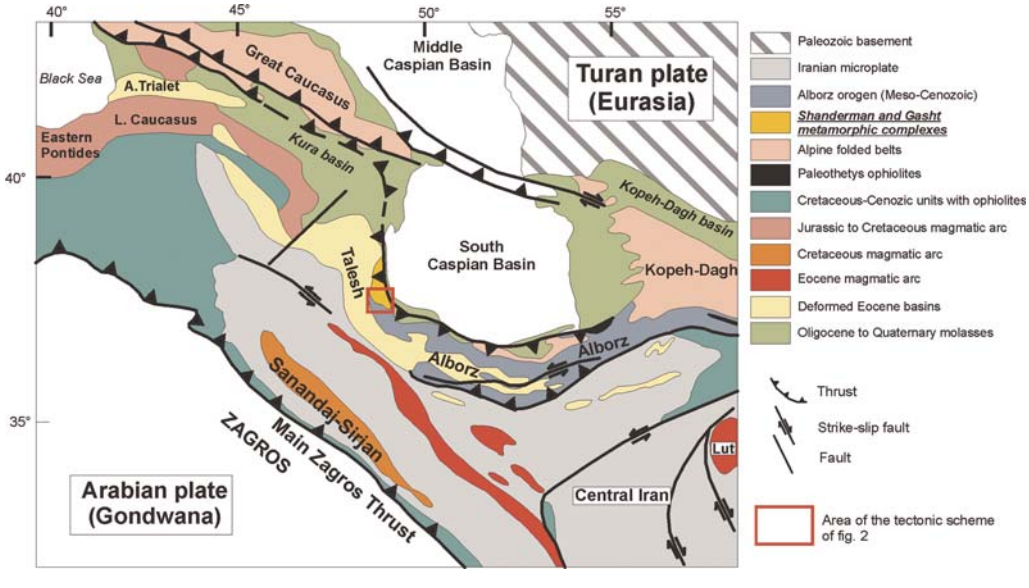


**Fig. 1.** Simplified tectonic map of the South Caspian region.

the Gasht and Shanderman complexes are exposed along the Caspian foothills of the belt. According to previous authors (Davies *et al.* 1972; Clark *et al.* 1975), this section of the Alborz belt records several distinct orogenic phases, from problematic Middle–Late Devonian tectono-metamorphic events to the Eo-Cimmerian orogeny, whose effects in the region are also described in detail in Zanchi *et al.* (2006, 2009). The Eo-Cimmerian event marking the collision of Iran with the southern margin of Eurasia is followed by a complex evolution, related to the opening of the 'palaeo-Caspian basin' through the Mesozoic and the beginning of the Cenozoic (Allen *et al.* 2002; Brunet *et al.* 2003, 2007). Compression dominated from Oligocene times, leading to the formation of the present-day mountain belt.

The metamorphic basement includes two poorly known units showing different evolutions and compositions (Fig. 2). The Shanderman Complex, that is the main subject of this paper, is later described in more detail. According to previous authors (Davies *et al.* 1972; Clark *et al.* 1975), it consists of an intricate association of phyllites, gneiss and amphibolites, with small patches of serpentinized peridotite, showing a medium-grade metamorphism. The peculiar composition of this unit has led several authors (Sengör 1984; Alavi 1996) to directly equate the Shanderman Complex to the ophiolitic succession of Mashad.

The Gasht Complex shows a different composition and evolution from the Shanderman basement; it includes two separate units showing a different metamorphic evolution. Phyllites with slates and quartzite form the upper unit, which is believed to unconformably cover the lower unit. According to Davies *et al.* (1972) a metaconglomeratic layer with kyanite-bearing clasts separates the two units. The lower unit, which is generally poorly exposed, consists of amphibolite-facies gneisses with sillimanite, kyanite and staurolite, with minor amounts of quartzites and amphibolites; the basement of the lower unit has later been intruded by granitoids. A greenschist-facies retrogression generally affects the unit. Middle–Late Devonian whole-rock Rb–Sr ages of $382 \pm 48$ and $375 \pm 12$ Ma have been obtained by Crawford (1977) on phyllite sampled near Masuleh. The whole complex was later intruded by Cimmerian granitic rocks, which have given an Early Jurassic radiometric age (175 Ma: Crawford 1977).

The Palaeozoic succession forms the axial part of the belt, consisting of Tertiary SW-vergent folds and thrust sheets, generally thrusted over the younger Meso-Cenozoic units. The Palaeozoic succession, which shows analogies with the units exposed in central-eastern Alborz and in Central Iran, has been related to the external part of the Gondwana-related Iranian plate by most authors (Davies *et al.* 1972; Clark *et al.* 1975; Stampfli *et al.* 1991), with a few exceptions (e.g. Wendt *et al.* 2005). A peculiar feature of the Talesh units is the occurrence of thick volcanic and volcaniclastic layers throughout the Palaeozoic and the occurrence of open-sea Orthoceras limestones in the Silurian beds. Permian units, where present, generally consist of fusulina-bearing limestone and marls. No Triassic carbonates are exposed in the Talesh Mountains. A thick succession of very-low-grade carbonates and metapelites with Upper Palaeozoic faunas (see also Zanchi *et al.* 2009), deformed during the Eo-Cimmerian orogeny, crops out in the central part of the belt. These units as well as the Gasht and Shanderman complexes are unconformably covered by the coal-bearing deltaic–shallow-marine siliciclastic deposits of the Shemshak Formation, that marks the growth and erosion of the Eo-Cimmerian orogen (Fürsich *et al.* 2009).

The basal Eo-Cimmerian 'molasse' is dated to the Norian in central Alborz, to the Sinemurian in the axial part of the Talesh Mountains, to the Aalenian northward (Clark *et al.* 1975; Seyed-Emami 2003; Ghasemi-Nejad *et al.* 2004). The composition of the basal conglomeratic layers of the Shemshak Formation suggests that the metamorphic units were exposed at the surface at the end of the Eo-Cimmerian orogeny.

The present-day complex structural setting was mainly acquired since Oligocene times and is defined by a system of imbricate SW-vergent thrust sheets exposing the Palaeozoic succession along ramp anticlines. North–south-trending right-lateral strike-slip faults favour the SW displacement of the thrust sheets, forming steep lateral ramps along the northern part of the belt. However, active faulting still occurs along the Caspian coast along a flat north–south thrust surface, which indicates eastwards thrusting of the belt on the South Caspian Sea (Allen *et al.* 2003). Left-lateral strike-slip motion to the south along a WNW–ESE active fault (Toram earthquake in Jackson *et al.* 2002) occurs in the Qezel Owzan Valley, south of the Talesh Mountains.

## Geological setting of the Shanderman Complex

The metamorphic and intrusive rocks of the Shanderman Complex crop out west of the towns of Shanderman and Masal along the deep valleys dissecting the eastern slopes of the Talesh Mountains. Isolated outcrops of metamorphic rocks are exposed northwards in small erosional windows below the Mesozoic sediments up to the town of Asalem. The structural position of this

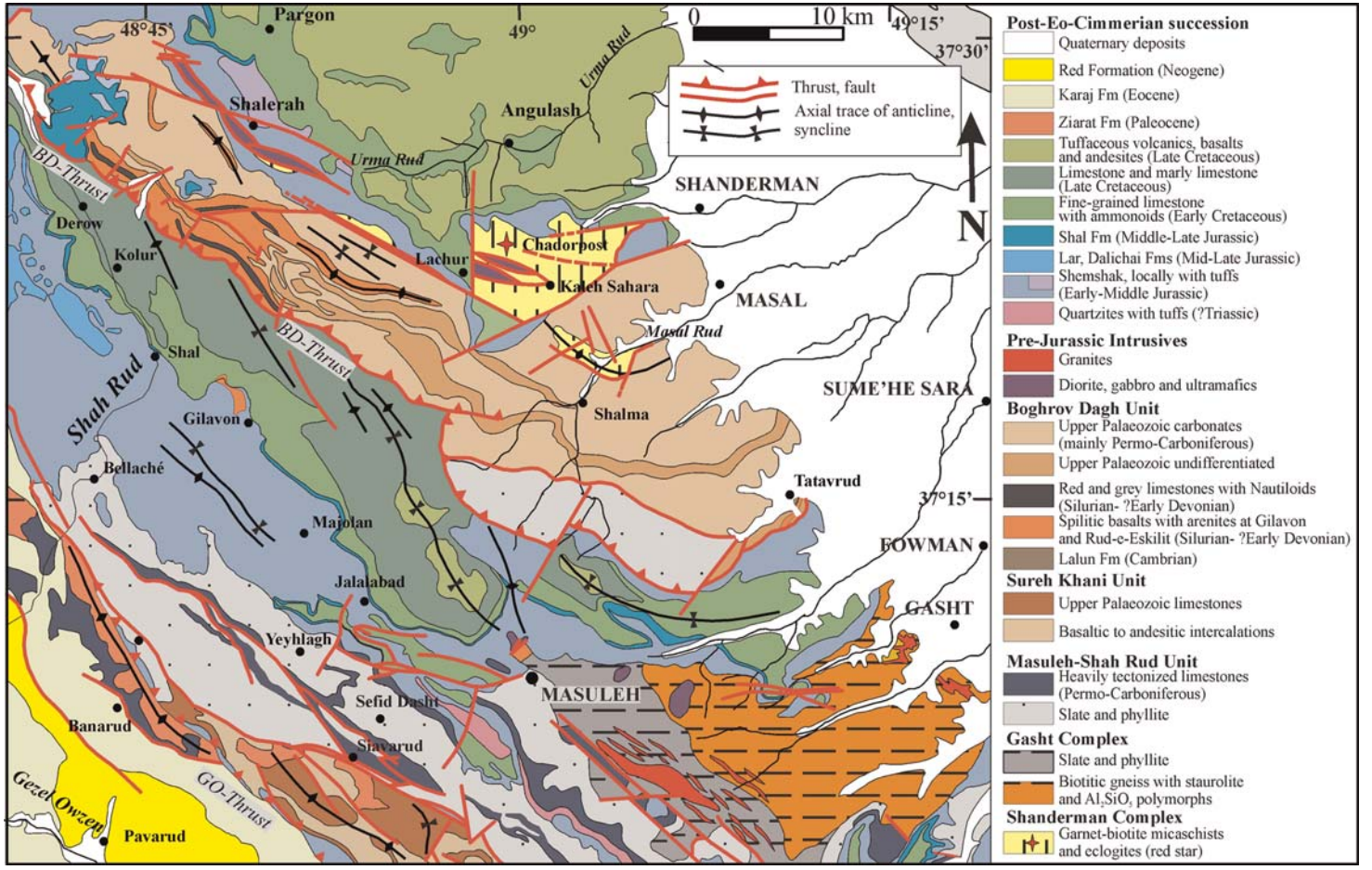


**Fig. 2.** Geological scheme of the NW Talesh Mountains region (detail from scheme of Fig. 1).

complex is ambiguous owing to the lack of significant exposures, as the Caspian foothills of the Talesh Mountains are, in fact, densely forested and rocks are deeply weathered. Strike-slip and normal faults generally separate these rocks from the Palaeozoic successions cropping out to the west, whereas between the Masal and Lachur valleys the Palaeozoic sedimentary successions seem to tectonically cover the basement along low-angle surfaces.

The Shanderman Complex mainly includes metabasites and micaschists, with only minor calcschists, quartzites and phyllites (Lachur Valley). Phyllitic rocks always show white mica porphyroclasts, suggesting that they have been originated by retrogression of the surrounding micaschists.

In the Masal Valley the crystalline basement of the Shanderman Complex is represented by partly retrogressed garnet–staurolite micaschists with minor amphibolites, present as metric-scale boudins, and quartzite levels. The metamorphic basement was successively intruded by intermediate–mafic intrusive bodies, rich in ultramafic cumulates, mainly exposed in the Lachur Valley and in the Urma Valley, near the village of Shalerah, where the intrusives form a NW–SE narrow fault-bounded stripe within micaschists and amphibolites.

Field structural analysis has shown the presence of at least three distinct deformational phases in the complex. The first phase produced a pervasive foliation under eclogitic conditions, the second one is responsible for crenulation of the previous structures, locally associated with an axial plane foliation, developed under amphibolite-facies conditions. The third deformation phase produces gentle–close folds with NW–SE-oriented axes and subvertical axial planes.

The whole complex is cross-cut by high-angle and vertical WNW–ESE- and NNW–SSE-trending shear zones, a few to several metres thick, with, respectively, left- and right-lateral motions. Rocks are deeply fractured and altered close to shear zones, showing a pervasive serpentinization of the ultramafics. Ultramafic cumulates are also heavily serpentinized along the contacts with the eclogites and micaschists. Contacts between the igneous bodies and the metamorphic rocks were not observed owing to poor exposure. We suppose, based on general geometrical relationship, that the boundary is a partially faulted primary intrusive contact.

## Structural evolution and petrography of the Shanderman metamorphic rocks

The metamorphic rocks of the Shanderman Complex consist of mafic eclogites, garnet amphibolites and micaschists, with minor amounts of calcschists, phyllites and quartzites. Eclogites are present as bodies, several tens to hundreds of metres in size, cropping out within garnet–staurolite–kyanite micaschists near the village of Chadorpost (star in Fig. 1), along the road taking to Lachur.

The metamorphic basement of the Shanderman Complex was affected by at least three different phases of ductile deformation. The first phase ($D_1$) is responsible for the development of a pervasive axial plane foliation ($S_1$) within the eclogites, marked by the preferred orientation of paragonite and clinopyroxene (Fig. 3a, d). The $S_1$ foliation is clearly visible only within the eclogitic bodies, whereas it has been almost completely transposed during the successive deformation phases in the surrounding micaschists. Rare and poorly preserved relicts of the $S_1$ foliation were observed at the microscale within garnet amphibolites, where pseudomorphs of plagioclase + amphibole symplectite on former omphacitic clinopyroxene define a weak preferred orientation at a high angle to the $S_2$ foliation developed during the amphibolite-facies retrogression.

The successive event ($D_2$) occurred at amphibolite-facies conditions. It is evident within micaschists and garnet amphibolites where an axial plane foliation, $S_2$, represents the most pervasive fabric element at the meso- and the microscale. The $D_2$ deformation phase did not deeply affect the eclogites, where only a weak crenulation of the $S_1$ eclogitic foliation is locally present.

The garnet amphibolites cropping out near the village of Varadeh and along the Lachur Valley are strongly foliated, with garnet present only as relicts. The foliation is defined by amphibole + titanite + zoisite and is pervasive on millimetric scale. In some samples a symplectitic association made of plagioclase + amphibole has been observed, suggesting a former eclogitic mineral assemblage for the garnet amphibolites. The pervasive foliation shown by the amphibolites is probably correlated to the crenulation observed in the eclogites, which post-dates the eclogitic event. Structural relationships between eclogites and amphibolites have not been observed, but the presence of plagioclase + diopside symplectites within the amphibolites suggest that the garnet amphibolites of Lachur and Varadeh have also experienced high-pressure conditions. Retrogression of the eclogitic assemblage in garnet amphibolites was accompanied by the development of a strong foliation, which is absent in well-preserved eclogite outcrops.

Foliation $S_2$ present in the garnet–kyanite–staurolite micaschists and the garnet amphibolites is locally intensively crenulated due to a successive deformation phase ($D_3$). $D_3$ is responsible for the development of tight–closed folds present both at

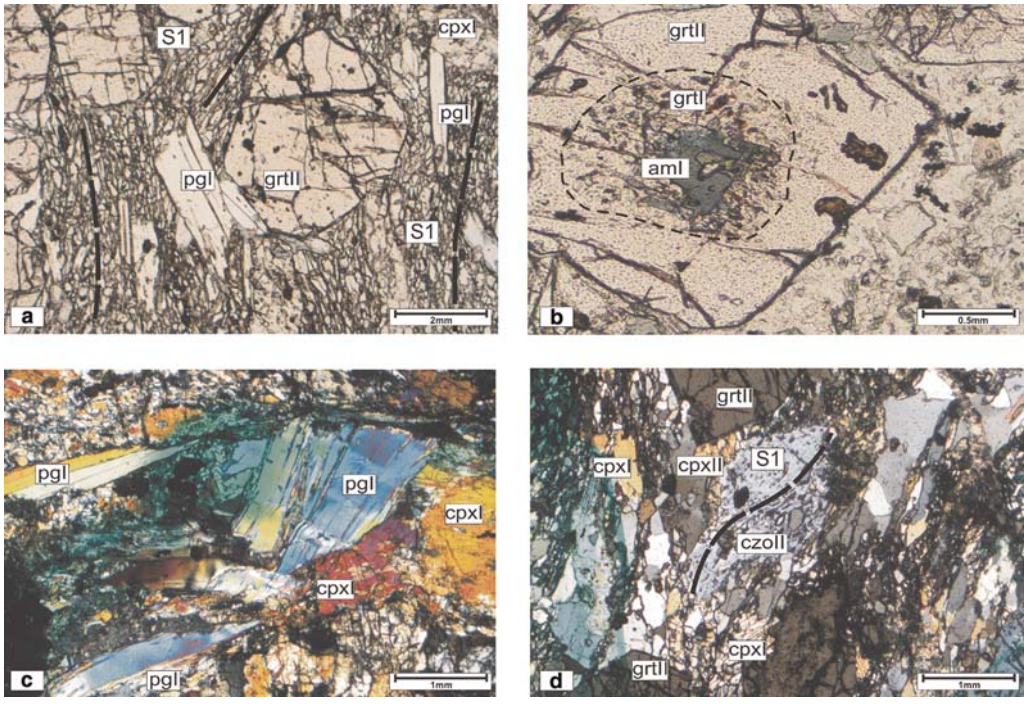


**Fig. 3.** Microstructures of the Shanderman eclogites. (**a**) Garnet (grtII) and paragonite (pgI) porphyroblasts in a fine-grained matrix made of cpxII + pgII + czoII. (**b**) Garnet porphyroblast preserving a core (grtI) with inclusions of bluish-green amphibole (amI), quartz, chlorite and rutile of the $M_1$ phase assemblage. (**c**) Large paragonite (pgI) and omphacitic clinopyroxene (cpxI) porphyroblasts of the $M_2$ eclogitic assemblage. (**d**) Clinozoisite porphyroblasts (czoII) synkinematic with respect to $S_1$ foliation; inclusions forming the internal foliation within the czoII crystals are of rutile, quartz and paragonite.

the cm- and the m-scale that are not associated to an axial plane foliation.

The contacts between the eclogites and the surrounding micaschists and amphibolites are generally covered. Thus, structural relationships between the eclogitic bodies and the surrounding basement remain unclear, even if the pressure peak recorded by the eclogites should predate the main deformation event, $D_2$, easily recognizable in micaschists and amphibolites. Nonetheless, a common tectono-metamorphic evolution of eclogites, garnet amphibolites and micaschists can be assumed, based on the occurrence of the $S_1$ relicts and of diopside + plagioclase symplectites within the garnet amphibolites, suggesting the derivation of these from former eclogites such as those exposed near Chadorpost.

The eclogites display a S-tectonitic texture owing to the preferred orientation of white mica and clinopyroxene that define a pervasive foliation, the $S_1$ in the above reconstruction. A poorly defined mineralogical layering is formed by mm-thick metamorphically differentiated garnet- or clinopyroxene-rich layers.

Eclogites have a rich mineralogy with clinopyroxene, garnet, paragonite, phengite, amphibole, clinozoisite, epidote, quartz, rutile, titanite, calcite, plagioclase, and minor apatite and chlorite.

The texture is generally inequigranular owing to the occurrence of porphyroblasts, some millimetres in size, of garnet, omphacite, clinozoisite and paragonite, surrounded by a pervasive foliation made of the same phases, with the exception of garnet and the addiction of quartz and rutile. Garnet porphyroblasts display an inclusion-rich core and a almost inclusion-free rim, that had partly overgrown the $S_1$ foliation. In the garnet cores inclusions of bluish-green amphibole, epidote, white mica, quartz, rutile and calcite were recognized.

Microstructural analyses allow the reconstruction of at least three different equilibrium-phase assemblages in the mafic eclogites of the Shanderman Complex. Mineral abbreviations in the text follow IUGS recommendations.

The first assemblage ($M_1$) is preserved within garnet cores and includes:

$$\text{amI} + \text{ep} + \text{phg} + \text{rt} + \text{qtz} + \text{cal} \pm \text{chl}(M_1).$$

This paragenesis is thought to predate the eclogite-facies stage and possibly indicates high-pressure–low-temperature conditions within the epidote–blueschist facies. Garnet cores (grtI) preserving this phase assemblage (Fig. 3b) display a rounded shape with irregular rims, often characterized by clusters of tiny rutile and quartz inclusions. Textural relationships occurring between garnet cores and the inclusions of the $M_1$ phase assemblage remain unclear, even if it is likely that grtI post-dates the growth of the $M_1$ assemblage and predate the successive eclogitic stage.

The successive phase assemblage ($M_2$) grew at eclogite-facies conditions and consists of:

$$\text{grtII} + \text{cpxI} + \text{pgI} + \text{czoI} + \text{qtz} + \text{rt} + \text{cal}\ (M_2).$$

GrtII rims grew in continuity on grtI cores, usually with a euhedral habit. CpxI, pgI, rtII, qtz and cc inclusions were rarely observed within grtII. Omphacitic clinopyroxene (cpxI) paragonite (pgI) and clinozoisite (czoII) are present as millimetric porphyroblasts displaying no shape-preferred orientation. CpxI and pgI porphyroblasts (Fig. 3c) are almost inclusion-free and clearly predate the development of the $S_1$ foliation. In several samples pgI porphyroblasts display evidence of recrystallization at the contacts with the fine-grained pgII, individuating the $S_1$ foliation. CzoI porphyroblasts preserve remnants of internal foliation made of qtz and rt, that is sometimes in continuity with $S_1$. Owing to these characters, czoI is considered pre- to early-$S_1$.

The $S_1$ foliation shows the same phase assemblage of the porphyroblast population and is made of fine-grained omphacitic clinopyroxene, paragonite, zoisite, quartz and rutile. Locally, garnet rims grew statically on the $S_1$ foliation indicating that garnet growth outlasts the formation of $S_1$. The sin-$S_1$ phase assemblage consists of:

$$\text{grtII} + \text{cpxII} + \text{pgII} + \text{czoII} + \text{qtz} \pm \text{ttn}\ (M_3).$$

Eclogites are exceptionally well preserved and only a few samples display a non-pervasive re-equilibration at amphibolite-facies conditions. In this case plgI + amII symplectites grew on cpxI and cpxII, whereas amII + plgII coronae formed around some garnet porphyroblasts. In a few cases tiny epidote crystals (epII) have been found within amII + plgII coronae around garnet. The presence of epidote in the phase assemblage, substituting for garnet, indicates pressure conditions below the garnet stability field, i.e. within the epidote–amphibolite facies. In two samples a greenschist-facies re-equilibration was observed with thin rims of actinolitic amphibole (amIII) and albite (amIII) growing on cpxI porphyroblasts.

## Whole-rock data of eclogites and mafic intrusives

The small plutons intruded into the Shanderman Complex are mainly Mg-gabbros, with minor ultramafic cumulates and rare acid differentiates. The intrusives are substantially undeformed and only slightly metamorphosed in greenschist-facies conditions. The magmatic texture is well preserved in most of the samples. The ultramafic cumulates are locally serpentinized, probably due to fluid circulation along various dm- to m-thick steep shear zones affecting the rocks. Supplementary material: GPS co-ordinates of the analysed samples are available in Table 1 at http://www.geolsoc.org.uk/SUP18342.

The primary magmatic phase assemblage of the gabbros is: clinopyroxene + plagioclase + amphibole + olivine + spinel. In some samples epidote seems to be a primary mineral, whereas more often it is recognized as a secondary phase grown on clinopyroxene and amphibole. The ultramafic cumulates are mainly made of clinopyroxene and olivine (i.e. wehrlitic in composition) with minor orthopyroxene.

Almost all the collected samples are olivine-normative (i.e. Mg-gabbros) and display a transitional–alkaline character based on major element whole-rock analyses (Fig. 4). The Kalhe–Sahara Gabbro displays a marked alkaline character with respect to the Lachur and Shalerah gabbros. The ultramafic cumulates plot in the gabbronorite field of the De La Roche diagram, i.e. towards the Mg-rich area. Supplementary material: whole-rock chemical data of the mafic intrusives, ultramafic cumulates and metabasites of the Shanderman Complex are available in Table 2 at http://www.geolsoc.org.uk/SUP18342. The high-field-strength (HFS) elements' abundances and ratios point to a volcanic arc as the most suited tectonic setting for the emplacement of the mafic intrusives. Oceanic character of the arc crust is unlikely in that continental crust has to be preferred owing to the presence of magmatic epidote, which indicates medium pressures of crystallization, compatible with a mid-crustal setting.

The rare earth element (REE) chondrite-normalized patterns of the gabbros (Fig. 5b) are similar for all the samples, except for the RA10

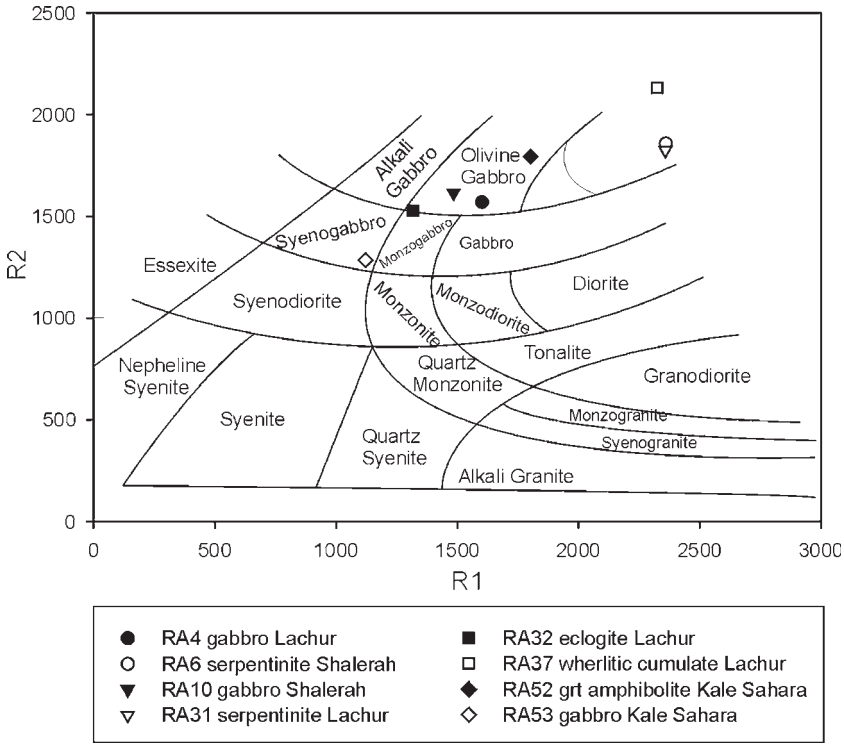


**Fig. 4.** R1–R2 classification diagram (De La Roche *et al.* 1980) of representative samples of the Shanderman eclogites and mafic intrusives. Eclogites (sample RA32) and most of the gabbros plot within the olivine gabbro field. Serpentinites from Shalerah and Lachur plot in the gabbronorite field.

(Shalerah Gabbro) which displays an evident enrichment in light REE (LREE) (about 80 times chondritic values for La and Ce) similar to ocean island basalt (OIB) or enriched mid-ocean ridge basalt (E-MORB).

The REE patterns of the other mafic intrusives and metabasites are of the normal MORB (N-MORB) type (Fig. 5b), with LREE less than 10 times chondritic values and the heavy REE (HREE) around or slightly above 10 times chondritic values. Interpretation of the incompatible element diagram is more difficult due to the enhanced dispersion of the values. Incompatible elements, and specially the large-ion lithophile elements (LILE), are known to be very mobile during metamorphism and hydrothermal alteration due to their high solubility in aqueous fluids. As the Shanderman intrusive rocks have been slightly metamorphosed at greenschist-facies conditions, and the circulation of aqueous fluid is demonstrated by the presence of serpentinized ultramafic cumulates, the interpretation of the incompatible element diagrams has to be considered tentative. The most evident differences lie in the LILE abundances with the Shalerah Gabbro enriched in LILE compared with the Lachur and the Kale Sahara gabbros (Fig. 5a). A more or less marked negative Nb anomaly is present in the pattern, compatible with the interpretation of a volcanic arc based on the HFSE (HFS element) content and ratios. Whole-rock chemical analyses have also been performed on the garnet amphibolites (RA52) and eclogites (RA32). The major element and the trace element data of the eclogites and amphibolites are very similar to those of the intrusive rocks analysed. The Kale Sahara amphibolites display marked positive anomalies of K and Sr; the origin of these LILE anomalies is not well understood and a possible metamorphic origin needs to be taken into account because of the high solubility of these elements in aqueous fluids.

## Mineral chemistry

Quantitative mineral analyses were obtained with an ARL SEMQ microprobe and a JEOL 8200 Superprobe at the University of Milan, both equipped with WDS spectrometers. Operating

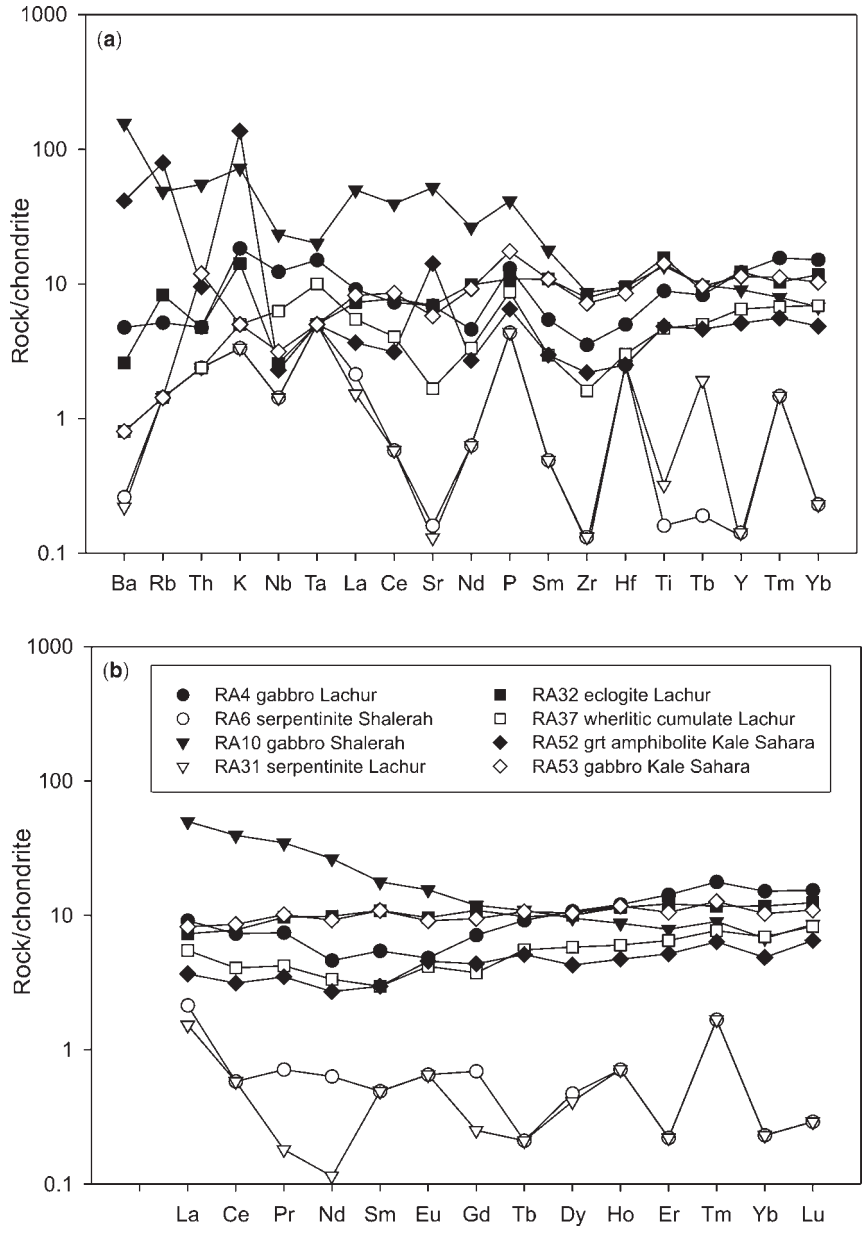


**Fig. 5.** (**a**) Incompatible and (**b**) REE spider diagrams of the Shanderman mafic intrusives and eclogites. Chondrite values are from Nakamura (1974).

conditions were 15 kV and 15 nA. Natural silicates were used as standards and the resulting data were processed with a ZAF (atomic number (Z), absorption (A) and fluorescence (F)) correction procedure. All the analyses were collected using a focused beam, except for the micas for which a 5 μm-probe diameter was used.

### *Garnet*

The chemical formulae of garnet were recalculated on the basis of 12 oxygens; the amount of $Fe^{3+}$ was determined by charge balance.

Garnet is mainly a Grs–Pyr–Alm solid solution, with the Sps component always <10%. Most

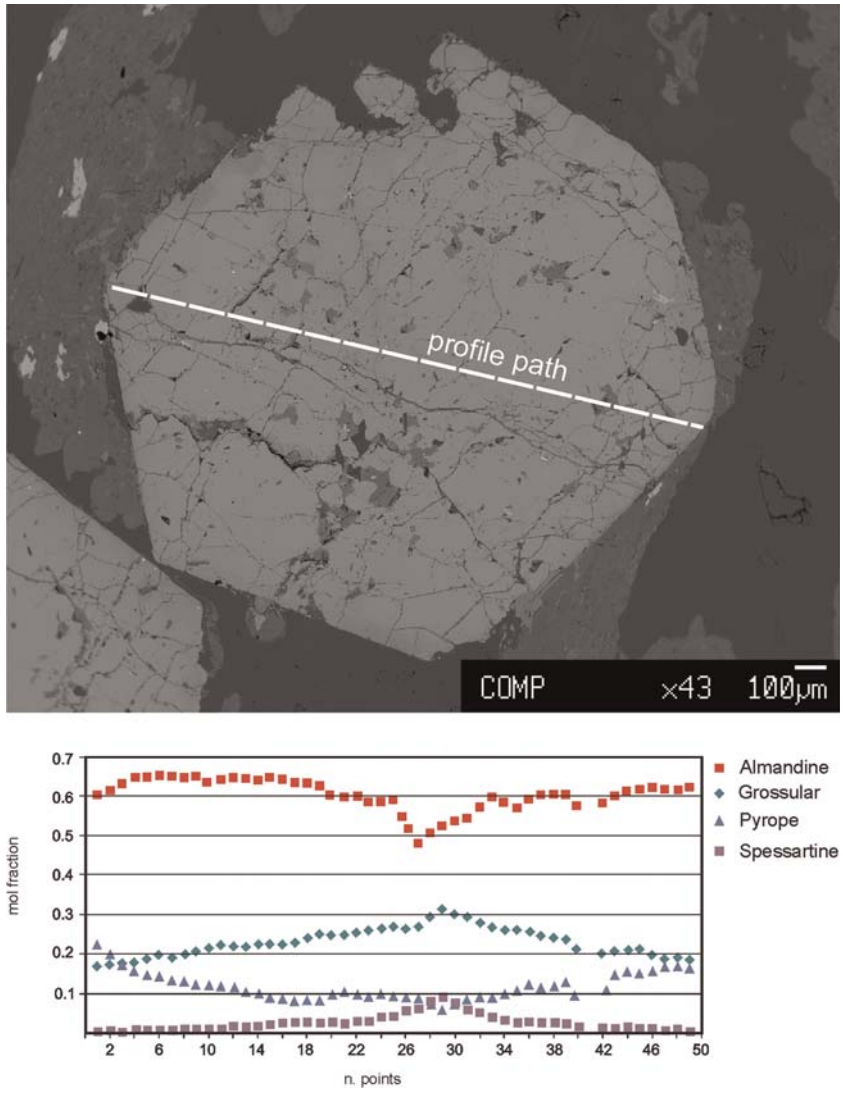


**Fig. 6.** Compositional profile through a garnet porphyroblast. Garnet shows a continuous chemical zoning with a core enriched in Grs and Sps. The Pyr and the Alm components increase towards the rim.

garnet porphyroblasts display a continuous zoning with a Grs- and a Pyr-rich core, and an enrichment of Alm and Pyr components towards the rim (Figs 6 and 7). Cores containing inclusions of blueschist-facies assemblage are $Alm_{49-62}Grs_{32-22}Pyr_{08-11}Sps_{10-05}$ in composition. Towards the rim Alm increases up to 65 mol%, Grs decreases below 20 mol% and the Pyr component reaches values of 20–22 mol%. Compositional profiles and X-rays maps indicate that all the analysed garnet porphyroblasts are continuously zoned, with no discontinuities at the contact between the blueschist-facies cores and the outer eclogitic rims. The continuous chemical zoning of garnet is supposed to be due to a re-equilibration during the eclogite-facies metamorphism that annealed previous chemical inhomogeneities or to a continuous garnet growth through the transition from blueschist to eclogitic conditions. Representative garnet microprobe data are listed in Table 1.

Supplementary material: a complete list of garnet microprobe data is available in Table 3 at http://www.geolsoc.org.uk/SUP18342.

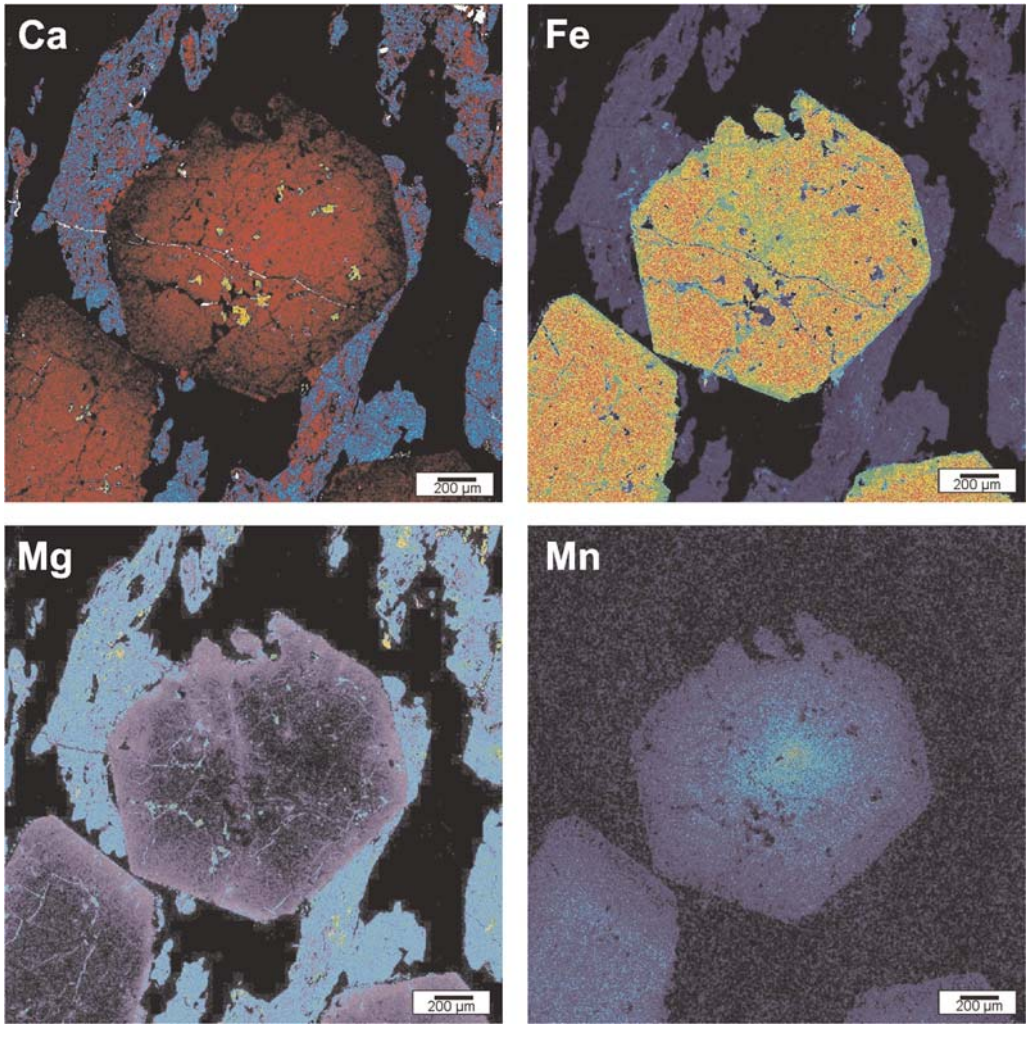


**Fig. 7.** Concentration maps of Ca, Mg, Fe and Mn within garnet. Maps were collected with a dwell time of 100 ms and are 1024 × 1024, with each pixel 3 × 3 μm in size.

### *Clinopyroxene*

Clinopyroxene analyses were recalculated on the basis of 6 oxygens, the amount of $Fe_2O_3$ was determined by stoichiometric charge balance.

Two different generations of clinopyroxene are present, both of them with omphacitic composition. CpxI porphyroblasts display a Na content ranging between $Jd_{45}$ and $Jd_{50}$, with $XMg(Fe_{tot})$ always close to 0.73. CpxI display a weak zoning with porphyroblast cores somewhat higher in Na content with respect to outer rims, with constant values of $Jd_{48-50}$ for the cores and $Jd_{45-49}$ for the rims (Fig. 8). CpxII, present within the foliated matrix ($S_1$ foliation), is also omphacitic in composition but with a lower Na content that ranges between $Jd_{40}$ and $Jd_{46}$. The $XMg(Fe_{tot})$ values are inhomogeneous, and range between 0.67 and 0.78. Representative electron microprobe analyses of clinopyroxenes from the Shanderman eclogites are given in Table 1. Supplementary material: chemical composition of omphacite from Shanderman eclogites are available in Table 4 at http://www.geolsoc.org.uk/SUP18342.

### *White mica*

White mica analyses were recalculated on the basis of 11 oxygens, considering all Fe as $Fe^{2+}$.

**Table 1.** *Representative microprobe analyses of eclogite facies minerals from the $M_2$ and $M_3$ phase assemblages*

| Sample | IR24 | RA32 | IR24 | RA32 | IR24 | RA32 | RA32 | RA32 | RA32 | IR24 | RA32 | IR24 | IR24 | IR24 |
|---|---|---|---|---|---|---|---|---|---|---|---|---|---|---|
| Stage | cpxI | cpxI | cpxII | cpxII | grt (core) | grt (rim) | wmcaI | pgI | pgII | amI | amI | ep | czoI | czoII |
| $SiO_2$ | 57.75 | 57.72 | 56.26 | 56.35 | 37.91 | 38.61 | 51.28 | 47.82 | 47.46 | 45.58 | 45.58 | 38.32 | 39.47 | 39.36 |
| $TiO_2$ | 0.06 | 0.00 | 0.04 | 0.07 | 0.11 | 0.06 | 0.16 | 0.05 | 0.05 | 0.46 | 0.46 | 0.02 | 0.11 | 0.25 |
| $Al_2O_3$ | 12.05 | 11.89 | 10.32 | 10.96 | 20.93 | 21.08 | 27.11 | 38.97 | 39.37 | 11.63 | 11.63 | 23.55 | 28.50 | 28.01 |
| $Cr_2O_3$ | 0.02 | 0.03 | 0.01 | 0.00 | 0.06 | 0.04 | 0.03 | 0.07 | 0.01 | 0.04 | 0.04 | 0.02 | 0.08 | 0.00 |
| $Fe_2O_3$ | 2.45 | 2.52 | 1.51 | 0.67 | 0.69 | 0.51 | – | – | – | 15.64 | 15.64 | 12.89 | 6.29 | 9.00 |
| FeO | 2.31 | 2.43 | 2.62 | 3.35 | 28.92 | 28.49 | 2.69 | 0.49 | 0.41 | 4.85 | 4.85 | – | – | – |
| MnO | 0.00 | 0.04 | 0.08 | 0.01 | 1.25 | 0.39 | 0.01 | 0.00 | 0.03 | 0.07 | 0.07 | 0.12 | 0.05 | 0.11 |
| MgO | 6.86 | 6.93 | 8.47 | 8.36 | 2.02 | 4.29 | 3.36 | 0.21 | 0.16 | 7.92 | 7.92 | 0.04 | 0.20 | 0.32 |
| CaO | 11.23 | 11.04 | 13.78 | 13.44 | 8.97 | 7.38 | 0.01 | 0.30 | 0.40 | 8.17 | 8.17 | 23.08 | 23.11 | 21.38 |
| $Na_2O$ | 8.23 | 8.21 | 6.83 | 6.87 | 0.01 | 0.01 | 0.78 | 6.85 | 7.04 | 3.74 | 3.74 | 0.01 | 0.01 | 0.03 |
| $K_2O$ | 0.01 | 0.01 | 0.01 | 0.00 | nd | nd | 9.79 | 0.93 | 0.57 | 0.12 | 0.12 | 0.00 | – | – |
| Total | 100.97 | 100.82 | 99.92 | 100.09 | 100.88 | 100.86 | 95.23 | 95.69 | 95.50 | 98.23 | 98.23 | 98.05 | 97.81 | 98.46 |
| Si | 2.02 | 2.02 | 2.00 | 2.00 | 3.00 | 3.01 | 3.42 | 3.04 | 3.02 | 6.61 | 6.49 | 3.04 | 3.05 | 3.03 |
| Ti | 0.00 | 0.00 | 0.00 | 0.00 | 0.01 | 0.00 | 0.01 | 0.00 | 0.00 | 0.05 | 0.07 | 0.00 | 0.01 | 0.01 |
| Al | 0.50 | 0.49 | 0.43 | 0.46 | 1.95 | 1.94 | 2.13 | 2.92 | 2.95 | 1.99 | 2.19 | 2.20 | 2.59 | 2.54 |
| Cr | 0.00 | 0.00 | 0.00 | 0.00 | 0.00 | 0.00 | 0.00 | 0.00 | 0.00 | 0.00 | 0.00 | 0.00 | 0.00 | 0.00 |
| $Fe^{3+}$ | 0.06 | 0.07 | 0.04 | 0.02 | 0.04 | 0.03 | – | – | – | 1.71 | 1.76 | 0.77 | 0.37 | 0.52 |
| $Fe^{2+}$ | 0.07 | 0.07 | 0.08 | 0.10 | 1.91 | 1.86 | 0.15 | 0.03 | 0.02 | 0.59 | 0.54 | – | – | – |
| Mn | 0.00 | 0.00 | 0.00 | 0.00 | 0.08 | 0.03 | 0.00 | 0.00 | 0.00 | 0.01 | 0.01 | 0.01 | 0.00 | 0.01 |
| Mg | 0.36 | 0.36 | 0.45 | 0.44 | 0.24 | 0.50 | 0.33 | 0.02 | 0.02 | 1.71 | 1.60 | 0.00 | 0.02 | 0.04 |
| Ca | 0.42 | 0.41 | 0.52 | 0.51 | 0.76 | 0.62 | 0.00 | 0.02 | 0.03 | 1.27 | 1.25 | 1.96 | 1.91 | 1.76 |
| Na | 0.56 | 0.56 | 0.47 | 0.47 | 0.00 | 0.00 | 0.10 | 0.84 | 0.87 | 1.05 | 1.09 | 0.00 | 0.00 | 0.01 |
| K | 0.00 | 0.00 | 0.00 | 0.00 | – | – | 0.83 | 0.08 | 0.05 | 0.02 | 0.02 | – | – | – |
| Cations | 3.98 | 3.98 | 4.00 | 4.00 | 8.00 | 7.99 | 6.14 | 6.88 | 6.91 | 15.00 | 15.00 | 7.98 | 7.96 | 7.92 |

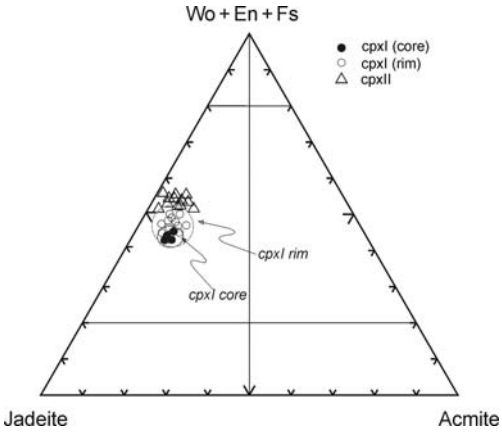


**Fig. 8.** Clinopyroxene compositions.

White mica, phg, preserved within garnet cores together with ampI, zoI, rt, qtz and cc (the $M_1$ phase assemblage) displays a phengitic composition with Si up to 3.4 pfu (per formula unit) and a constant $XMgFe^{2+}$ of 0.68–0.69. Paragonite porphyroblasts, pgI, have a K/Na ratio comprised between 0.09 and 0.11, with $XMgFe^{2+}$ ranging from 0.43 to 0.51, with the higher values usually in the cores. PgII, the white mica that defines the $S_1$ foliation, displays a similar composition with somewhat lower K/Na ratio (0.05–0.9) and similar $XMgFe^{2+}$. The Ca content of paragonite ranges between 0.25 and 0.30 pfu for pgI, and between 0.25 and 0.40 for pgII. Representative white mica analyses from the eclogites are given in Table 1 and are available as supplementary material in Table 5 at http://www.geolsoc.org.uk/SUP18342.

## *Amphibole*

Amphibole analyses were recalculated on the basis of 23 oxygens and 13 cations + K + Na + Ca.

AmI, preserved within garnet cores, is barroisitic in composition with Na content ranging between 1.01 and 1.41 apfu (atoms per formula unit), which means a Na amount in the B site between 0.72 and 1.03 pfu (Fig. 9a).

In some cases amI inclusions in garnet display a weak zoning, with Na content decreasing towards the rims. $XMgFe_{(tot)}$ values range between 0.40 and 0.43. AmII formed during amphibolite-facies re-equilibration, and it is present together with plagioclase within symplectites on former omphacitic clinopyroxene, cpxI and cpxII, or within amphibole–plagioclase coronae around garnet porphyroblasts. AmII is tschermakitic in composition with high $XMg(Fe^{2+})$, usually >0.75, and with symplectitic amphiboles displaying the higher values up to 0.90 (Fig. 9b). In several samples a thin rim of actinolitic amphibole, amIII, was observed around omphacitic clinopyroxene. A few amphibole analyses are reported in Table 1. Supplementary material: a more complete list of amphibole analyses from Shanderman eclogites is available in Table 6 at http://www.geolsoc.org.uk/SUP18342.

## *Epidotes*

Epidote analyses were recalculated on the basis of 12.5 oxygens considering all Fe as $Fe^{3+}$.

Epidote (ep) preserved within garnet cores belong to the $M_1$ blueschist-facies assemblage, and show a $Fe^{3+}$ content between 0.75 and 0.80 pfu with no Mn (Mn < 0.02 pfu). CzoI and czoII show a similar composition, with no Mn (Mn < 0.03 pfu) and $Fe^{3+}$ ranging between 0.37 and 0.45 pfu, with czoI displaying invariably the lower values, 0.37–0.40, and czoII the higher ones, 0.40–0.45. Representative analyses of different epidote generations are listed in Table 1 and are available as supplementary material in Table 7 at http://www.geolsoc.org.uk/SUP18342.

## *Other minerals*

Plagioclase formulae were recalculated on the basis of 8 oxygens pfu. PlgI and plgII occurring with amphibole in symplectites around garnet, display a similar composition with An content around 0.15–0.18 mol%. The third generation of plagioclase, plgIII, supposed to have grown during the latest stages of exhumation display an albitic composition, with Ab = 97 mol%.

Chlorite is present within garnet cores and it is supposed to belong to the $M_1$ blueschist-facies-phase assemblage. Chlorite compositions are represented by clinochlore–daphnite solid solutions, with minor deviations towards the sudoite end-member. The mean $X_{Mg}$ values range between 0.50 and 0.61, with the exception of chlorites from the RA32 sample which display lower $X_{Mg}$, within the range of 0.39–0.47.

Titanite, rutile, apatite and rare ilmenite have been found as inclusions in garnet and in the matrix without any significant compositional variations. Chemical formulae of titanite were recalculated considering all Fe as $Fe^{3+}$ (Oberti *et al.* 1991). The $X_{Al}$ of titanite, where $X_{Al} = Al/(Al + Ti + Fe^{3+})$, is low and has constant values of 0.04–0.06.

Supplementary material: analyses of plagioclase, chlorite and titanite from the Shanderman eclogites are available in Table 8 at http://www.geolsoc.org.uk/SUP18342.

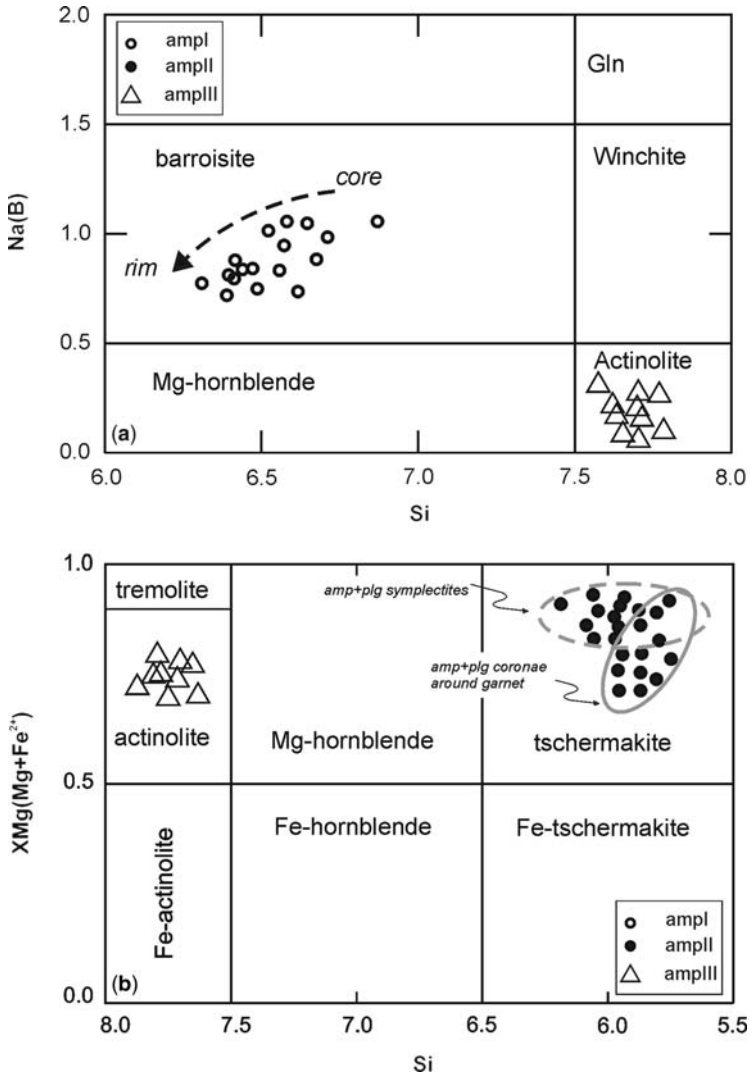


**Fig. 9.** (**a**) Na content in the B site v. Si content of amphibole. (**b**) $X_{Mg}$ v. Si content. Amphibole classification on both diagrams is after Leake *et al.* (1997).

## Metamorphic evolution of the Shanderman eclogites

Pressure–temperature equilibrium conditions of the different metamorphic phase assemblages in the paragonite-bearing eclogites of the Shanderman Complex were estimated by means of available geothermometers and geobarometers, with additional constraints from available experimental data.

The peculiarity of the Shanderman eclogites is the preservation of a prograde $P$–$T$ path from the blueschist to the eclogite facies. The $M_1$ phase assemblage, aml + ep + phg + rt + qtz + cc ± chl, indicates high-pressure–low-temperature conditions roughly constrained to 0.7–1.1 GPa at temperatures of 400–550 °C.

The pressure interval is defined on the basis of experimentally determined (Maruyama *et al.* 1986) and calculated (Evans 1990; Kerrick & Connolly 2001) mafic blueschist-phase relations, which indicate the disappearance of albite with increasing pressure in favour of sodic-amphibole + clinozoisite/epidote-bearing assemblages at 0.6–0.8 GPa in a temperature range of 400–500 °C. The absence of sodic-clinopyroxene in the $M_1$

assemblage indicates equilibrium pressure below 1.1 GPa at 400–550 °C.

Constraining the equilibrium temperature for the $M_1$ phase assemblages is more difficult owing to the absence of reliable indicators. Considering garnet cores that preserve $M_1$ inclusions not in equilibrium with them, the maximum temperature for the $M_1$ stage is constrained by the garnet-in reactions, with increasing temperature within the 0.6–1.1 GPa pressure range, that sets an upper temperature limit for the $M_1$ assemblage of around 450–500 °C (Maruyama *et al.* 1986; Evans 1990; Okay *et al.* 1998).

A successive pressure increase resolved in the stabilization of eclogitic conditions at which both $M_2$ and $M_3$ phase assemblages have grown. The $M_2$ and $M_3$ assemblages are both characterized by the absence of amphibole and the presence of paragonite, together with garnet, Na-clinopyroxene, clinozoisite, calcite, quartz, rutile ($M_2$) and titanite ($M_3$).

Experimentally determined phase relations on $H_2O$-saturated MORB-like systems (Schmidt & Poli 1998; Poli & Schmidt 2004) constrain well the $P$–$T$ stability field of amphibole-absent and clinozoisite/zoisite-bearing eclogitic-phase assemblages. Amphibole breaks down with increasing pressure at 2.4–2.5 GPa in the 530–700 °C temperature range, whereas (clino)zoisite is stable up to 3.1 GPa at approximately 700 °C (Poli & Schmidt 1995) for bulk-rock compositions with normative anorthite content (CIPW norm) around 31 wt%. The absence of amphibole in the $M_2$ and $M_3$ eclogitic-phase assemblages of the Shanderman eclogites could possibly represent a lower pressure limit for the pressure peak, whereas the presence of (clino)zoisite is not so indicative due to the dependence of epidote stability on the normative anorthite content of the rock. An increased $an^{CIPW}$ content results in a much larger pressure range for epidote stability (Thompson & Ellis 1994; Wittenberg *et al.* 2002; Poli & Schmidt 2004) both towards upper and lower pressures. The $an^{CIPW}$ content of the Shanderman eclogites ranges between 33 and 34.5 wt%, so it is slightly higher than the 31 wt% $an^{CIPW}$ of Poli & Schmidt (1995), probably resulting in a higher than 3.1 GPa pressure limit for (clino)zoisite within $M_2$ and $M_3$ phase assemblage of the Shanderman eclogites. Suggested equilibrium pressure for the $M_2$ and $M_3$ phase assemblages consider as indicative the absence of amphibole, even if it may also be due to compositional effect. If this is the case 2.4–2.5 GPa has to be taken as the maximum pressure, whereas a lower pressure limit is provided by the stability of paragonite (Holland 1979), as discussed below.

The upper pressure boundaries for equilibrium conditions of the $M_2$ and $M_3$ phase assemblages can be derived by the presence of paragonite in equilibrium with garnet, clinopyroxene and clinozoisite.

The paragonite-out reaction in Figure 10 is derived from Holland (1979): the paragonite breakdown, with a negative $dP/dT$ slope, constrains the $M_2$ and the $M_3$ equilibrium paragenesis at pressure below approximately 2.5 GPa for temperatures between 530 and 650 °C. Following previous considerations and considering as indicative the absence of amphibole, the presence of paragonite brackets the pressure peak recorded by the

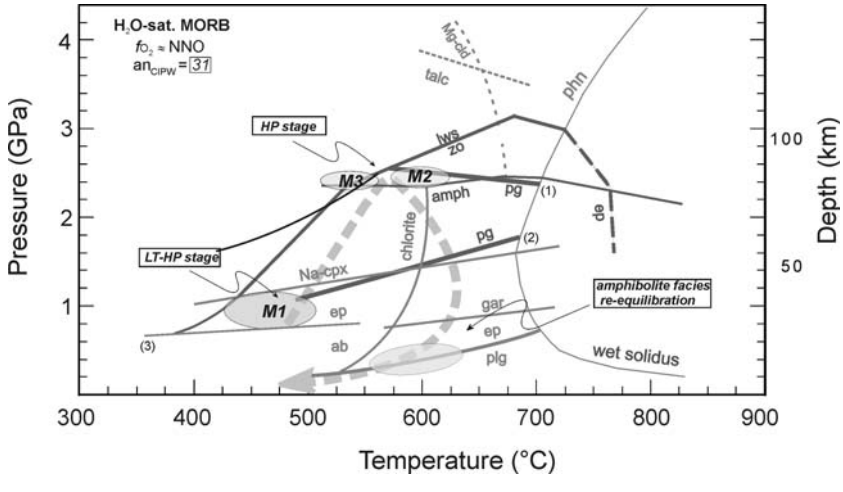


**Fig. 10.** Phase relations in hydrated MORB-like compositions (with $an^{CIPW} = 31$ wt%) with emphasis on (clino)zoisite-, epidote- and paragonite-bearing equilibria (Poli & Schmidt 2004). Reaction (1) and (2) are from Holland (1979); reaction (3) from Apted & Liou (1983). The $P$–$T$ equilibrium fields for the $M_1$, $M_2$ and $M_3$ phase assemblages of the Shanderman eclogites are shaded in grey.

Shanderman eclogites at 2.3–2.5 GPa. The grossular content of garnet coexisting with zoisite and omphacitic clinopyroxene in the $M_2$ and $M_3$ assemblages is similar to those reported by several experimental data (Poli & Schmidt 1995; Molina & Poli 2000) for pressure in the range of 2–2.5 GPa and bulk compositions approaching that of the Shanderman eclogites, this represents an additional constraint supporting the lower pressure estimate in addition to the absence of amphibole.

Temperature estimates for the $M_2$ and $M_3$ phase assemblages have been obtained by the garnet–clinopyroxene $Fe^{2+}$–Mg exchange geothermometer. Three different calibration have been applied: Ai (1994), Berman *et al.* (1995) and Krogh Ravna (2000). Supplementary material: analyses of the garnet–clinopyroxene pairs used for *T* estimates are available in Table 9 at http://www.geolsoc.org.uk/SUP18342 together with results in Table 10 at http://www.geolsoc.org.uk/SUP18342. Equilibrium temperatures obtained with the Ai (1994) and Krogh Ravna (2000) calibrations are lower with respect to those obtained employing the Berman *et al.* (1995) thermometer (Fig. 11). For pressures ranging between 2.3 and 2.5 GPa, the Ai (1994) and Krogh Ravna (2000) thermometers result in 510–560 °C for the $M_2$ phase assemblage and 440–490 °C for the $M_3$ phase assemblage. Temperatures obtained with the Berman *et al.* (1995) calibration are 50–60 °C higher than the previous and fit better with the experimentally determined phase relations represented in Figure 10. The temperatures obtained with the Ai (1994) and Krogh Ravna (2000) thermometers indicate equilibrium conditions for the $M_2$ stage and, especially, the $M_3$ stage close or within the lawsonite stability field. As no evidence of lawsonite growth has been observed, results obtained with the Berman *et al.* (1995) calibration of the garnet–clinopyroxene Fe–Mg exchange thermometer have to be considered more reliable than estimates made with the Ai (1994) and Krogh Ravna (2000) calibrations. Discrepancies between the three different calibrations arise from the different $dP/dT$ slope of $K_D$ curves, with the Berman *et al.* (1995) calibration displaying a steeper slope compared with the other two. Such a difference results in minor discrepancies at high temperature, where the three calibrations give similar results (Krogh Ravna 2000), but at lower temperature the gap increases up to 60–70 °C. Following previous considerations, reliable temperature estimates for the $M_2$ and $M_3$ eclogitic-phase assemblages are, respectively, 575–615 and 505–550 °C.

Pressure–temperature estimates of the eclogitic assemblages indicate that the $M_3$ stage occurred at lower temperature and lower pressure than the $M_2$. The pressure indication is derived from the jadeite content of cpxII (*c*. 0.45), belonging to $M_3$, which is somewhat lower than that of cpxI (*c*. 0.50) in the $M_2$ assemblage.

After the pressure peak some eclogite samples display a non-pervasive re-equilibration at epidote–amphibolite-facies conditions. Plagioclase–amphibole symplectites substituted for omphacitic clinopyroxene and amphibole + plagioclase ± epidote formed around garnet porphyroblasts.

Epidote coexisting with plagioclase within coronae around garnets provides textural evidence of equilibrium pressures in the range of 0.4–0.8 GPa (Apted & Liou 1983). Temperature estimates for the re-equilibration stage have been performed with the amphibole–plagioclase thermometer of Holland & Blundy (1994) on amII and plgII substituting for garnet: estimates range between 550 and 630 °C for that pressure range. The latest stages of exhumation are recorded by the rare presence of actinolitic rims on omphacitic clinopyroxene, sometimes coexisting with albite and

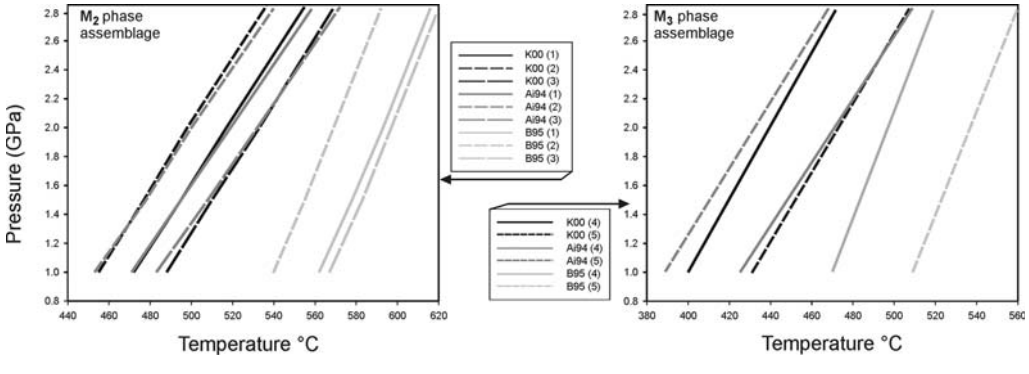


**Fig. 11.** Temperature estimates for the grt–cpx pairs of the $M_2$ and $M_3$ phase assemblage. Ai94, Ai (1994); B95, Berman *et al.* (1995); K00: Krogh Ravna (2000).

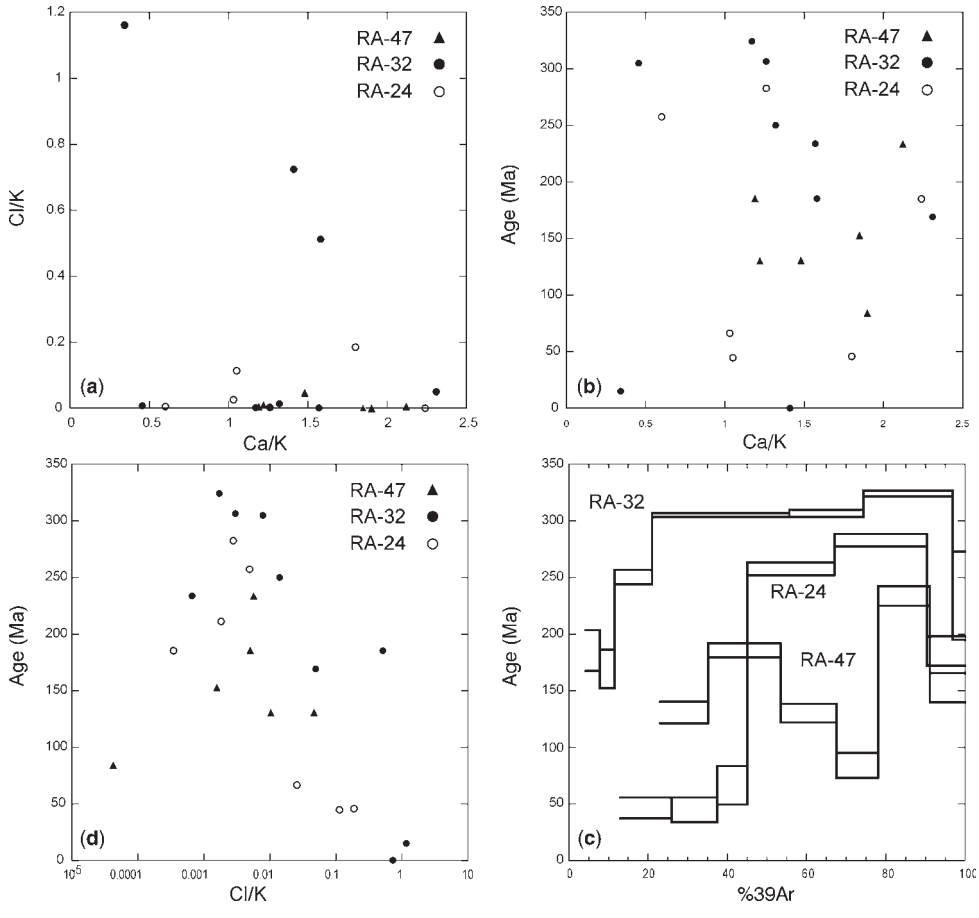


**Fig. 12.** (**a**) Ca/K v. Cl/K ratios of white mica separates from the Shanderman eclogites. (**b**) Ca/K v. step ages diagram. The Ca/K ratio of the less retrogressed samples, RA32 and RA24, plot in a narrow interval ranging between 1.17 and 1.26. (**c**) Cl/K ratios v. step ages. (**d**) Age spectrum diagram obtained by stepwise heating of paragonite separates of the Shanderman eclogites. The least altered sample, RA32, displays three steps, amounting to 76% gas release, ranging between 305 $\pm$ 2 and 324 $\pm$ 3 Ma.

by chlorite grown along fractures in garnet porphyroblasts.

## Geochronology

Three paragonite samples were analysed using $^{39}Ar-^{40}Ar$ stepwise heating. Samples were separated using heavy liquids and purified by handpicking under the microscope. Owing to sample size limitations, heterogeneities in the obtained separates could not be eliminated. These heterogeneities derive to a great extent from intergrown retrogression products, as discussed in the petrographic description.

In order to unravel the isotopic signal of mixtures, the classic tool is the use of three-isotope common-denominator correlation diagrams (Villa 2001), because the minerals composing the mixture degas at different temperatures. As paragonite contains Ca in its stoichiometric formula, the most natural choice is use of the Ca/K ratio as abscissa and as ordinate the Cl/K ratio (a monitor of alteration) or step ages (Fig. 12a, b). The Ca/K v. age diagram was successfully used by Tomaschek *et al.* (2003) to estimate an age for a paragonite–phengite mixture. In Figure 12a, it can be seen that the data points for all three samples define a V-shape: one branch corresponds to variable Ca/K ratios with low Cl/K ratio, while a few points show an anticorrelated increase of Cl/K for decreasing Ca/K ratios. Such a distribution requires at least three different Ar reservoirs. A possible interpretation would identify the high-Cl, low-Ca points as alteration phases of the original Ca-rich

paragonite. The low-Ca, low-Cl points would represent a different alteration or impurity phase different from paragonite. Because the points of all three samples define similar V-shaped trajectories, we are encouraged to believe that while their relative mass balance varies amongst our samples, the identity of the non-paragonite contaminants is the same and reflects the same retrogression/alteration event.

In Figure 12b, it can be seen that the step ages for the two less retrogressed samples, RA24 and RA32, correspond to Ca/K ratios in the narrow interval between 1.17 and 1.26. We interpret this ratio as the chemical signature of paragonite and the corresponding ages as those least affected by chemical perturbations.

The influence of alteration on ages can be diagnosed using the Cl/K v. age diagram (Fig. 12c). This plot was used by Heuberger *et al.* (2007) to resolve the effect of secondary modification of a substoichiometric muscovite. For all three samples, the highest step ages correspond to Cl/K ratios between 0.002 and 0.008, a range of values that is typical of white micas. Alteration results in introduction of Cl and removal of Ar, as shown by the negative correlation slope shown by our data points. Extreme Cl/K ratios exceeding 1 correspond to almost zero-age secondary phases. On the left-hand side of the diagram, each sample features one high temperature step with low ratios $<0.0008$. These could correspond to minor admixtures/intergrowths of a late-degassing, Cl-free phase such as (secondary young) feldspar.

The age spectrum diagram (Fig. 12d) can now be reliably interpreted in terms of multiple generations of variably altered minerals. The least altered sample is RA-32, which features three steps (totalling 76% of the gas release) ranging between $305 \pm 2$ and $324 \pm 3$ Ma. Given the mutual discordance of these three steps, a conservative age estimate for the paragonite-forming metamorphism is $315 \pm 9$ Ma.

## Discussion and conclusions

Our data support the interpretation of the Shanderman Complex as a deeply subducted slice of continental crust intruded during exhumation by intermediate–mafic intrusives, in places rich in ultramafic cumulates. Pressure–temperature estimates made on paragonite-bearing mafic eclogites point to peak metamorphic conditions up to 2.3–2.5 GPa at 575–615 °C ($M_2$ phase assemblage) indicating a subduction depth of 70–80 km. In several samples, pre-eclogitic phase assemblages ($M_1$) are well preserved within garnet cores and are thought to record first stages of subduction at 0.7–1.1 GPa and 400–550 °C within the epidote–blueschist facies. Successive re-equilibration occurred within the epidote–amphibolite facies at 0.4–0.8 GPa and 550–630 °C. The consensus of the data set indicates a clockwise $P$–$T$–$t$ path for the Shanderman eclogites with a minor cooling event, represented by the transition from stage $M_2$ to $M_3$, before the onset of exhumation.

$^{39}Ar$–$^{40}Ar$ radiometric dating of paragonites belonging to the $M_2$ and $M_3$ phase assemblages gives a minimum age for the eclogite-facies metamorphism of $315 \pm 9$ Ma, indicating that the metamorphic basement of the Shanderman Complex was subducted to crustal depths during the Late Carboniferous.

Whole-rock data of mafic intrusives and ultramafic cumulates of the Lachur, Masal and Urma valleys, intruded within the metamorphics of the Shanderman Complex, display a transitional to continental affinity, possibly related to a volcanic arc setting. The intrusives are only slightly metamorphosed, with local serpentinization of ultramafic cumulates occurring along shear zones, and weak and a non-pervasive greenschist metamorphic overprint present on gabbros and diorites. Such data indicate that the intrusion occurred probably after or during the amphibolite-facies re-equilibration recorded by the eclogites and micaschists of the Shanderman basement.

The conclusion contrasts with the commonly accepted interpretation of the Shanderman Complex as part of an ophiolitic belt delineating the Palaeothetys suture extending from the Talesh Mountains of NW Iran eastwards to the ophiolites of the Mashad–Binalood Complex (Sengör 1984; Alavi 1996). Our data suggest the metamorphic basement of the Shanderman Complex is a part of a Palaeozoic orogenic belt, the remnants of which are presently exposed within the Shanderman Complex itself and the Gasht Complex (Davies *et al.* 1972; Clark *et al.* 1975; Crawford 1977).

Several lines of evidence point to relevant orogenic activity occurring during the Carboniferous in the Transcaucasian region along the southern part of the Lesser Caucasus (Sengör 1990). In the Dzirula Massif of the Transcaucasian region, high-grade gneisses, amphibolites and migmatites at the external boundaries of the Chorchana–Utslevi Zone are intruded by 'Variscan granitoids', with K/Ar ages mainly clustering in the Late Carboniferous (Adamia *et al.* 1983). Silurian–Devonian phyllites, gabbros, metavolcanics and sheared serpentinites with Cambrian marble slivers, possibly representing a dismembered ophiolite unit, form the Chorcana–Utslevi Zone, which also shows Late Carboniferous Rb/Sr ages for the metapelites. A similar succession is exposed further east in the Khrami Salient and Loki Massif, where

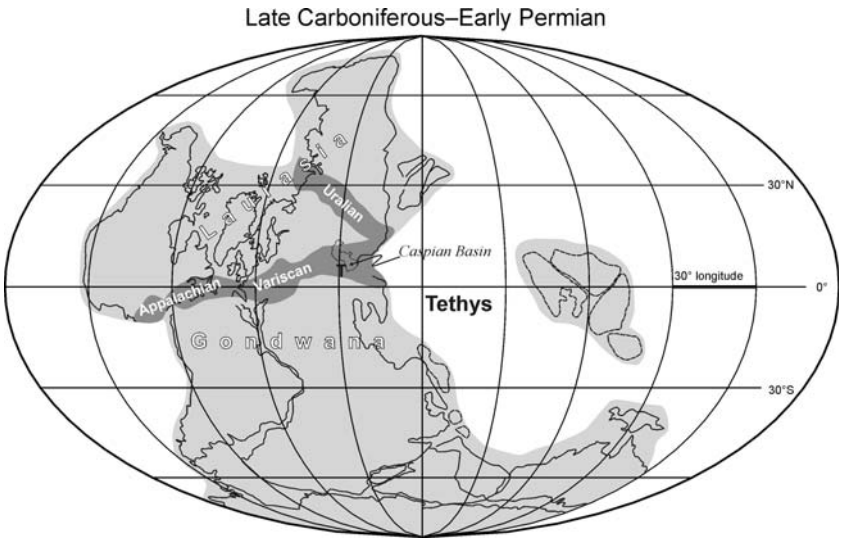


**Fig. 13.** Late Carboniferous–Early Permian reconstruction of Pangea obtained by using paleomagnetic poles and Euler poles of rotation for Gondwana and Laurasia outlined in Angiolini *et al.* (2007). The Transcaucasian region (T), locus of origin of the Shanderman Complex, is indicated. See the text for discussion.

medium- to high-grade gneisses and greenschist to epidote–amphibolite metamorphic rocks are, respectively, intruded by Lower Carboniferous and Upper Carboniferous granitoids. K/Ar ages of $287 \pm 15$, $319 \pm 11$ and $333 \pm 11$ Ma have been obtained on muscovites from the metamorphics of the Loki Massif (Abesadze *et al.* 1982). Similar ages spanning from 325 to 338 Ma come from the granites intruding the metamorphic basement. Moreover, high-pressure eclogitic rocks, Late Devonian–Carboniferous in age (Philippot *et al.* 2001; Kazmin 2006; Saintot *et al.* 2006), also occur to the north of the Great Caucasus range. To the south and east of the Black Sea, evidence of a Late Palaeozoic orogenic event are still widespread as testified by the occurrence of high-grade (amphibolite–granulite facies) metamorphic basement rocks in the Pulur, Devrekani, Uludağ and Kazdağ massifs of the Sakarya Zone of the Eastern and Central Pontides (Okay *et al.* 2006; Topuz *et al.* 2007). Isotopic ages from high-grade gneisses constrain the age of metamorphism of the Pulur and Kazdağ massifs to 300–330 Ma (Okay *et al.* 2006 and references therein). Other evidence of Carboniferous orogenic activity has also been reported recently from the Jandaq metamorphic complex (Bagheri & Stampfli 2008) in central Iran, south of the Great Kavir Fault, where Ar/Ar mica ages from greenschists and amphibolites give a 320–333 Ma age for the main metamorphic event.

In order to gauge the plate tectonic scenario responsible for the Late Palaeozoic age of the high-pressure metamorphism recorded in the Shanderman Complex, we reconstructed the configuration of Pangea using selected palaeomagnetic data of Late Carboniferous–Early Permian age from stable Africa and Europe, as outlined in Angiolini *et al.* (2007). This Late Carboniferous–Early Permian Pangea is remarkably similar to Pangea B of Irving (1977) and Morel & Irving (1981), with Africa placed south of Asia and South America south of Europe (Fig. 13), as also confirmed for the Permian by subsequent palaeomagnetic analyses (Muttoni *et al.* 1996, 2003; Torcq *et al.* 1997; Irving 2005). Pangea B transformed into a more classic Wegenerian A-type configuration, with Africa immediately south of Europe and South America south of North America, by means of a dextral motion of Laurasia relative to Gondwana that took place during the Early Permian broadly along the Variscan suture (Muttoni *et al.* 2003, 2004).

An increasing body of biogeographical and geological data seems to support Pangea B and its transformation to a Pangea A-type configuration during the Permian (Angiolini *et al.* 2007; Muttoni *et al.*, submitted). Focusing on arguments more pertinent to this study, Pangea B provides a symmetrical framework for the Appalachian–Variscan fold belt, placing the Appalachians of eastern North America opposite to the northwestern South America fold belt, and the Variscan fold belt of Europe opposite to the northwestern Africa fold belt of the Mauritanides, as originally noticed by Irving (1977) and Morel & Irving (1981). Within Pangea B, Carboniferous high-pressure deformation

of the Shanderman Complex finds a logical geodynamic context of Variscan convergence of Gondwana relative to Laurasia, which would otherwise be far from obvious assuming instead Variscan convergence in a Pangea A-type configuration where the Paleotethys Ocean bounded to the south the European margin at the longitudes of Transcaucasia.

The high-pressure metamorphic event of Transcaucasia was related by different authors to the accretion of a microplate, termed Makera-Pontus/Transcaucasia, to the European margin of the Scythian Platform. This microplate has been interpreted as a block possibly detached from Gondwana at the beginning of the Palaeozoic (Kazmin 2006), or alternatively as a Europe-related rifted fragment belonging to the southern margin of the Scythian Platform (Saintot *et al.* 2006). Acknowledging these hypotheses, we propose as an alternative and somewhat easier solution to interpret this and other compressional events of Late Paleozoic age as due to the convergence of Gondwana relative to Laurasia in a Pangea B-type configuration.

The Shanderman Complex can thus represent an allocthonous nappe coming from the southern margin of the Transcaucasian region, locus of original Variscan deformation. The nappe was displaced southwards and exhumed during the Eo-Cimmerian orogenesis after being stacked above the northern margin of the Iranian Plate. Its present position was acquired during the late Tertiary formation of the western Alborz belt and especially during the Neogene, when dextral shearing was active along north–south- to NNE–SSW-trending faults, which formed the lateral ramps of the SW-vergent fronts of the main thrust sheets present in the Iranian side of the Talesh Mountains. This event, which is responsible for the sinuous shape of the Talesh Mountains, produced a southwards displacement of the crystalline nappe stack now exposed along the Caspian foothills.

This work was funded by the MEBE project (proposal 02–26, Meso-Cenozoic Evolution of the Alborz Mountain Range, Iran) and by an Italian MURST PRIN Project (2004–2006, leader A. Zanchi) in collaboration with the Geological Survey of Iran. Dr M. R. Ghasemi, Dr A. Saidi and his colleagues of the Geological Survey of Iran are warmly thanked for continuous help and logistics. S. Andò helped in the separation of paragonites for Ar/Ar dating. Reviews by A. I. Okay and B. Lombardo greatly improved a first version of the manuscript.

## References

ABESADZE, M., ADAMIA, S. A., CHIKOTUA, T., KEKELIA, M., SHAVISHVILI, I., SOMIN, M. & TSIMAKURIDZE, G. 1982. Pre-Variscan and Variscan metamorphic complexes of the Caucasus (a review). IGCP, Project No. 5. *Newsletter*, **4**, 5–12.

ADAMIA, S. A., KEKELIA, M. & TSIMAKURIDZE, G. 1983. Pre-Variscan and Variscan granitoids of the Caucasus. IGCP, Project No. 5. *Newsletter*, **5**, 5–12.

AI, Y. 1994. A revision of the garnet–clinopyroxene $Fe^{2+}$–Mg exchange geothermometer. *Contributions to Mineralogy and Petrology*, **115**, 467–473.

ALAVI, M. 1991. Sedimentary and structural characteristics of the Paleo-Tethys remnants in northeastern Iran. *Geological Society of American Bulletin*, **103**, 983–992.

ALAVI, M. 1996. Tectonostratigraphic synthesis and structural style of the Alborz Mountain System in Iran. *Journal of Geodynamics*, **21**(1), 1–33.

ALAVI, M., VAZIR, H., SEYED-EMAMI, K. & LASEMI, Y. 1997. The Triassic and associated rocks of the Nakhlak and Aghdarband areas in central and northeastern Iran as remnants of the southern Turanian active continental margin. *Geological Society of America Bulletin*, **109**, 1563–1575.

ALLEN, M. B., JONES, S., ISMAIL-ZADEH, A., SIMMONS, M. & ANDERSON, L. 2002. Onset of subduction as the cause of rapid Pliocene–Quaternary subsidence in the South Caspian basin. *Geology*, **30**, 775–778.

ALLEN, M. B., VINCENT, S. J., ALSOP, G. I., ISMAIL-ZADEH, I. & FLECKER, R. 2003. Late Cenozoic deformation in the South Caspian region: effects of a rigid basement block within a collision zone. *Tectonophysics*, **366**, 223–239.

ANGIOLINI, L., GAETANI, M., MUTTONI, G., STEPHENSON, M. H. & ZANCHI, A. 2007. Tethyan oceanic currents and climate gradients 300 m.y. ago. *Geology*, **35**, 1071–1074.

APTED, M. J. & LIOU, J. G. 1983. Phase relations among greenschists, epidote–amphibolite, and amphibolite in a basalt system. *American Journal of Science*, **283A**, 328–354.

BAGHERI, S. & STAMPFLI, G. M. 2008. The Anarak, Jandaq and Posht-e-Badam metamorphic complexes in central Iran: New geological data, relationships and tectonic implications. *Tectonophysics*, **451**(1–4), 123–155.

BERBERIAN, M. & KING, G. 1981. Toward a paleogeography and tectonic evolution of Iran. *Canadian Journal of Earth Sciences*, **18**, 210–265.

BERMAN, R. G., ARANOVICH, L. & PATTISON, D. R. M. 1995. Reassessment of the garnet-clinopyroxene Fe–Mg exchange thermometer: II. Thermodynamic analysis. *Contributions to Mineralogy and Petrology*, **119**, 30–42.

BRUNET, M.-F., KOROTAEV, M. V., ERSHOV, A. V. & NIKISHIN, A. M. 2003. The South Caspian Basin: a review of its evolution from subsidence modelling. *Sedimentary Geology*, **156**, 119–148.

BRUNET, M.-F., SHAHIDI, A., BARRIER, E., MULLER, C. & SAÏDI, A. 2007. Geodynamics of the South Caspian Basin southern margin now inverted in Alborz and Kopet Dagh (Northern Iran). *In*: *European Geosciences Union EGU, General Assembly*, Vienna, Austria, 16–20 April 2007. *Geophysical Research Abstracts*, **9**, 08080.

CLARK, G. C., DAVIES, R. G., HAMZEPOUR, G. & JONES, C. R. 1975. *Explanatory Text of the Bandar-e-Pahlavi Quadrangle Map*, scale 1:250 000. Geological Survey of Iran, Tehran.

CRAWFORD, M. A. 1977. A summary of isotopic age data for Iran, Pakistan and India. *In*: *Livre à la mémoire de A. F. de Lapparent*. Société Géologique de France, Memoir, **8**, 251–260.

DAVIES, R. G., JONES, C. R., HAMZEPOUR, B. & CLARK, G. C. 1972. *Geology of the Masuleh Sheet, NW Iran, scale*, 1:100 000. Geological Survey of Iran, Report, **24**.

DE LA ROCHE, H., LETERRIER, J., GRANDCLAUDE, P. & MARCHAL, M. 1980. A classification of volcanic and plutonic rocks using R1–R2 diagram and major element analyses – its relationships with current nomenclature. *Chemical Geology*, **29**, 183–210.

EVANS, D. W. 1990. Phase relations of epidote blueschists. *Lithos*, **25**, 3–23.

FÜRSICH, F. T., WILMSEN, M., SEYED-EMAMI, K. & MAJIDIFARD, M. R. 2009. Lithostratigraphy of the Upper Triassic–Middle Jurassic Shemshak Group of Northern Iran. *In*: BRUNET, M.-F., WILMSEN, M. & GRANATH, J. W. (eds) *South Caspian to Central Iran Basins*. Geological Society, London, Special Publications, **312**, 129–160.

GHASEMI-NEJAD, E., AGHA-NABATI, A. & DABIRI, O. 2004. Late Triassic dinoflagellate cysts from the base of the Shemshak Group in north of Alborz Mountains, Iran. *Review of Palaeobotany and Palynology*, **132**, 207–217.

HEUBERGER, S., SCHALTEGGER, U., BURG, J.-P., VILLA, I. M., FRANK, M., DAWOOD, H., HUSSAIN, S. *ET AL*. 2007. Age and isotopic constraints on magmatism along the Karakoram–Kohistan Suture Zone, NW-Pakistan: Evidence for subduction and continued convergence after India–Asia collision. *Swiss Journal of Geosciences*, **100**, 85–107.

HOLLAND, T. J. B. 1979. Experimental determination of the reaction paragonite = jadeite + kyanite + $H_2O$ and internally consistent thermodynamic data for part of the system $Na_2O$–$Al_2O_3$–$SiO_2$–$H_2O$ with application to eclogites and blueschists. *Contribution to Mineralogy and Petrology*, **68**, 293–301.

HOLLAND, T. J. B. & BLUNDY, J. 1994. Non-ideal interactions in calcic amphiboles and their bearing on amphibole–plagioclase thermometry. *Contributions to Mineralogy and Petrology*, **116**, 433–447.

IRVING, E. 1977. Drift of the major continental blocks since the Devonian. *Nature*, **270**, 304–309; doi: 10.1038/270304a0.

IRVING, E. 2005. The role of latitude in mobilism debates. *National Academy of Sciences Proceedings*, **102**, 1821–1828; doi: 10.1073/pnas.0408162101.

JACKSON, J., PRIESTLEY, K., ALLEN, M. & BERBERIAN, M. 2002. Active tectonics of the South Caspian Basin. *Geophysical Journal International*, **148**, 214–245.

KAZMIN, V. G. 2006. Tectonic evolution of the Caucasus and Fore-Caucasus in the Late Paleozoic. *Doklady Earth Sciences*, **406**, 1–3.

KERRICK, D. M. & CONNOLLY, J. A. D. 2001. Metamorphic devolatilization of subducted oceanic metabasalts: implications for seismicity, arc magmatism and volatiles recycling. *Earth and Planetary Science Letters*, **189**, 19–29.

KROGH RAVNA, E. 2000. The garnet–clinopyroxene $Fe^{2+}$–Mg geothermometer: an updated calibration. *Journal of Metamorphic Geology*, **18**, 211–219.

LEAKE, B. E., WOLLEY, A. R. *ET AL*. 1997. Nomenclature of amphiboles. Report of the Subcommittee on Amphiboles of the International Mineralogical Association Commission on New Minerals and Minerals Names. *European Journal of Mineralogy*, **9**, 623–651.

MARUYAMA, S., CHO, M. & LIOU, J. G. 1986. Experimental investigations of blueschist–greenschist transition equilibria: pressure dependence of $Al_2O_3$ contents in sodic amphiboles – a new geobarometer. *In*: EVANS, B. W. & BROWN, E. H. (eds) *Blueschists and Eclogites*. Geological Society of America, Memoir, **164**, 1–6.

MOLINA, J. F. & POLI, S. 2000. Carbonate stability and fluid composition in subducted oceanic crust: an experimental study on $H_2O$–$CO_2$-bearing basalts. *Earth and Planetary Science Letters*, **176**, 295–310.

MOREL, P. & IRVING, E. 1981. Paleomagnetism and the evolution of Pangea. *Journal of Geophysical Research*, **86**, 1858–1872.

MUTTONI, G., GAETANI, M. *ET AL*. Neotethys opening and the Pangea B to Pangea A transformation during the Permian. *GeoArabia*, submitted.

MUTTONI, G., KENT, D. V. & CHANNELL, J. E. T. 1996. Evolution of Pangea: Paleomagnetic constraints from the Southern Alps, Italy. *Earth and Planetary Science Letters*, **140**, 97–112.

MUTTONI, G., KENT, D. V., GARZANTI, E., BRACK, P., ABRAHAMSEN, N. & GAETANI, M. 2003. Early Permian Pangea 'B' to Late Permian Pangea 'A'. *Earth and Planetary Science Letters*, **215**, 379–394.

MUTTONI, G., KENT, D. V., GARZANTI, E., BRACK, P., ABRAHAMSEN, N. & GAETANI, M. 2004. Erratum to "Early Permian Pangea 'B' to Late Permian Pangea 'A'" [*Earth Planet. Sci. Lett.* **215** (2003) 379–394]. *Earth and Planetary Science Letters*, **218**, 539–540.

MUTTONI, G., MATTEI, M., BALINI, M., ZANCHI, A., GAETANI, M. & BERRA, F. 2009. The drift history of Iran from the Ordovician to the Triassic. *In*: BRUNET, M.-F., WILMSEN, M. & GRANATH, J. W. (eds) *South Caspian to Central Iran Basins*. Geological Society, London, Special Publications, **312**, 7–29.

NAKAMURA, N. 1974. Determination of REE, Ba, Fe, Mg, Na and K in carbonaceous and ordinary chondrites. *Geochimica & Cosmochimica Acta*, **38**, 757–775.

OBERTI, R., SMITH, D. C., ROSSI, G. & CAUCIA, F. 1991. The crystal chemistry of high-aluminium titanites. *European Journal of Mineralogy*, **3**, 777–792.

OKAY, A. I., HARRIS, N. B. W. & KELLEY, S. P. 1998. Exhumation of blueschists along a Tethyan suture in the northwest Turkey. *Tectonophysics*, **285**, 275–299.

OKAY, A. I., SATIR, M. & SIEBEL, W. 2006. Pre-Alpide Palaeozoic and Mesozoic orogenic events in the

Eastern Mediterranean region. *In*: GEE, D. G. & STEPHENSON, R. A. (eds) *European Lithosphere Dynamics*. Geological Society, London, Memoirs, **32**, 389–406.

PHILIPPOT, P., BLICHERT-TOFT, J., PERCHUK, A., COSTA, S. & GERASIMOV, V. 2001. Lu–Hf and Ar–Ar chronometry supports extreme rate of subduction zone metamorphism deduced from geospeedometry. *Tectonophysics*, **342**, 23–38.

POLI, S. & SCHMIDT, M. W. 1995. $H_2O$ transport and release in subduction zones – experimental constraints on basaltic and andesitic systems. *Journal of Geophysical Research*, **100**, 22299–22314.

POLI, S. & SCHMIDT, M. W. 2004. Experimental subsolidus studies on epidote minerals. *Reviews in Mineralogy and Geochemistry*, **56**, 320–345.

RUTTNER, A. W. 1993. Southern borderland of Triassic Laurasia in north-east Iran. *Geologische Rundschau*, **82**, 110–120.

SAINTOT, A., STEPHENSON, R. A., STOVBA, S., BRUNET, M.-F., YEGOROVA, T. & STAROSTENKO, V. 2006. The evolution of the southern margin of Eastern Europe (Eastern European and Scythian platforms) from the latest Precambrian–Early Palaeozoic to the Early Cretaceous. *In*: GEE, D. G. & STEPHENSON, R. A. (eds) *European Lithosphere Dynamics*. Geological Society, London, Memoirs, **32**, 481–505.

SCHMIDT, M. W. & POLI, S. 1998. Experimentally based water budget for dehydrating slabs and consequences for arc magma generation. *Earth and Planetary Science Letters*, **163**, 361–379.

SCHMIDT, M. W. & POLI, S. 2004. Magmatic epidote. *Reviews in Mineralogy and Geochemistry*, **56**, 346–372.

SENGÖR, A. M. C. 1979. Mid-Mesozoic closure of Permo-Triassic Tethys and its implications. *Nature*, **279**, 590–593.

SENGÖR, A. M. C. 1984. *The Cimmeride Orogenic System and the Tectonics of Eurasia*. Geological Society of America, Special Paper, **195**.

SENGÖR, A. M. C. 1990. A new model for the late Palaeozoic–Mesozoic tectonic evolution of Iran and implications fro Oman. *In*: ROBERTSON, A. H., SEARLE, M. P. & RIES, A. C. (eds) *The Geology and Tectonics of the Oman Region*. Geological Society, London, Special Publications, **49**, 797–831.

SEYED-EMAMI, K. 2003. Triassic in Iran. *Facies*, **48**, 95–106.

STAMPFLI, G. M., MARCOUX, J. & BAUD, A. 1991. Tethyan margins in space and time. *Palaeogeography, Palaeoclimatology, Palaeoecology*, **87**, 373–409.

STÖCKLIN, J. 1968. Structural history and tectonics of Iran: a review. *AAPG Bulletin*, **52**, 1229–1258.

STÖCKLIN, J. 1974. Possible ancient continental margins in Iran. *In*: BURK, C. A. & DRAKE, C. L. (eds) *The Geology of Continental Margins*. Springer, Berlin, 873–887.

THOMPSON, A. B. & ELLIS, D. J. 1994. $CaO + MgO + Al_2O_3 + SiO_2 + H_2O$ to 35 kb – amphibole, talc and zoisite dehydration and melting reactions in tha silica-excess part of the system and their possible significance in subduction zones, amphibolite melting and magma fractionation. *American Journal of Science*, **294**, 1229–1289.

TOMASCHEK, F., KENNEDY, A., VILLA, I. M., LAGOS, M. & BALLHAUS, C. 2003. Zircons from Syros, Cyclades, Greece – Recrystallization and mobilization of zircon during high pressure metamorphism. *Journal of Petrology*, **44**, 1977–2002.

TOPUZ, G., ALTHERR, R., SCHWARZ, W. H., DOKUZ, A. & MEYER, H. P. 2007. Variscan amphibolite-facies rocks from the Kurtoğlu metamorphic complex (Gümüşhane area, Eastern Pontides, Turkey). *International Journal of Earth Sciences*, **96**, 861–873.

TORCQ, F., BESSE, J., VASLET, D., MARCOUX, J., RICOU, L. E., HALAWANI, M. & BASAHEL, M. 1997. Paleomagnetic results from Saudi Arabia and the Permo-Triassic Pangea configuration. *Earth and Planetary Science Letters*, **148**, 553–567; doi: 10.1016/S0012-821X(97)00047-2.

VILLA, I. M. 2001. Radiogenic isotopes in fluid inclusions. *Lithos*, **55**, 115–124.

VINCENT, S. J., ALLEN, M. B., ISMAIL-ZADEH, A. D., FLECKER, R., FOLAND, K. A. & SIMMONS, M. D. 2005. Insights from the Talysh of Azerbaijan into the Paleogene evolution of the South Caspian region. *Geological Society of America Bulletin*, **117**, (11/12), 1513–1533; doi: 10.1130/B25690.

WENDT, J., KAUFMANN, B., BELKA, Z., FARSAN, N. & BAVANDPUR, A. K. 2005. Devonian/Lower Carbonifeous stratigraphy, facies patterns and palaeogeography of Iran Part II. Northern and Central Iran. *Acta Geologica Polonica*, **55**(1), 31–97.

WITTENBERG, A., SCHLUSSER, J. & KOEPKE, J. 2002. Kinetic studies on the trace element distribution Ca–Al-rich silicates. *Geochimica and Cosmochimica Acta*, **66**(15A), A841–A841 Supplement.

ZANCHI, A., BERRA, F., MATTEI, M., GHASSEMI, M. & SABOURI, J. 2006. Inversion tectonics in Central Alborz, Iran. *Journal of Structural Geology*, **28**, 2023–2037.

ZANCHI, A., ZANCHETTA, S. *ET AL.* 2009. The Eo-Cimmerian (Late? Triassic) orogeny in North Iran. *In*: BRUNET, M.-F., WILMSEN, M. & GRANATH, J. W. (eds) *South Caspian to Central Iran Basins*. Geological Society, London, Special Publications, **312**, 31–55.